Wind-induced barotropic oscillations around the Saint Pierre and Miquelon archipelago (North-West Atlantic)

M Bezaud, P. Lazure, Bernard Le Cann

Wind-induced barotropic oscillations around the Saint Pierre and Miquelon archipelago (North-west Atlantic)

M. Bezaud[1], P. Lazure[1], B. Le Cann[2]

[1] Ifremer, Laboratoire d'Océanographie physique et Spatiale (LOPS), IUEM, Brest.
[2] CNRS, Laboratoire d'Océanographie physique et Spatiale (LOPS), IUEM, Brest.

Correspondence to: Marion Bezaud (marion.bezaud@ifremer.fr)

Key words

-Barotropic modelling

-Wind induced oscillations

-Continental Shelf Wave

-Saint Pierre and Miquelon Archipelago

-Newfoundland

Abstract.

We investigate the nearly barotropic oscillations recently observed around the Saint Pierre and Miquelon (SPM) archipelago. They were recorded by two ADCPs at about 30 m depth during winter and spring 2014. These oscillations were the dominant signal on the currents with a period of 2 to 4 days. Our analysis shows that these oscillations were triggered by the wind. To investigate these oscillations, a 2D numerical model was implemented at a regional scale. The results from a realistic simulation confirmed the impact of wind forcing on ocean dynamics in the region. They also showed amplification of these oscillations around SPM, particularly in the north-west of the archipelago and near Burin Peninsula. Analyses suggested the influence of continental shelf wave dynamics at a 'regional' scale. This regional wave then triggers a 'local' scale continental shelf wave propagating anticyclonically around SPM in ~2 days. Schematic modelling simulations with periodic wind stress forcing and relaxation after a gust of wind show a strong current response in this region with a wind stress periodicity centred around 2 days, which is attributed to resonance in the SPM area.

1. Introduction

The Saint Pierre and Miquelon (SPM) archipelago is located in the North-west Atlantic Ocean (Fig. 1) at the intersection of three regions which have been extensively studied (e.g. Han et al., 1999): the Grand Banks (located south-east of Newfoundland Fig. 1a) (e.g. Han, 2011), the Gulf of Saint Lawrence (e.g. Han et al., 2000, Han and Loder, 2003) and the Nova Scotian Shelf (e.g. Sandstrom, 1980). At the regional scale, the variability of the Labrador Current affects the dynamics of the Newfoundland and Scotian shelves and slopes (e.g. Chapman and Beardsley, 1989). Typically, the Labrador Current is composed of two equatorward flowing branches: an offshore component on the slope (Wu et al., 2012) and an inshore component that follows the topography around banks and channels. Each branch has a different temporal variability (e.g. Han, 2008, Wang et al., 2015). According to observations (e.g. Petrie, 1983, Hay and de Young, 1989) and hydrodynamical models (e.g. Urrego-Blanco and Sheng, 2012, Wang et al., 2015), the inshore Labrador Current flows between SPM and Newfoundland and has a major influence on the water properties in this area.

The ocean dynamics at frequencies from a few hours to a few days over the shelves of Newfoundland and Nova Scotia are partly driven by tides (Han and Loder, 2003, Han et al., 2010). In this region, the barotropic tide is mostly dominated by the semi-diurnal

components (Dupont et al., 2002). However, the barotropic tidal currents exhibit strong diurnal components in some locations near the edge of the continental shelf of Newfoundland, in the vicinity of St. Pierre Bank (Fig. 1a) (Xu and Loder, 2004) and around SPM (Lazure et al., 2018).

In autumn and winter, the dynamics in the region of Newfoundland are also driven by meteorological (mostly wind) events (e.g. Sandstrom, 1980, Wu et al., 2011). The impact of the wind on the ocean in this region has been studied extensively using *in situ* and remotely sensed data (e.g. Schwing, 1992a, Thiebaut and Vennell, 2010, Han, 2012). Other modelling studies have assessed the ocean response to storms using 2D (e.g. Schwing, 1989, Schwing, 1992b, Tang et al., 1998), and 3D modelling (e.g. Li et al., 2015, Ma et al., 2015). The studies on Nova Scotian shelf (Schwing, 1989, Schwing, 1992a, Schwing, 1992b) showed 2-day oscillations after wind events. On the Newfoundland shelf the wind events triggered Continental Shelf Waves (CSWs) which propagated equatorward (Tang et al., 1998, Thiebaut and Vennell, 2010, Han, 2012, Ma et al., 2015). Moreover a recent study (Li et al., 2015) showed the impact of storms on the Newfoundland shelf and emphasized strong surface and bottom currents in the vicinity of SPM and SPB (St. Pierre Bank (Fig. 1b)).

The predominant wind direction is from the west-south-west, based on measurements taken west of Fortune Bay (FB Fig. 1b) between 1994 and 2003 (Donnet et al., 2018). There are seasonal variabilities: in winter (December to February), the wind is mostly from the west to north and, in early spring (March-April) from west and south-west with a smaller component of the wind from the north (Donnet et al., 2018). There are two major storm tracks in the region: storms coming from the Rocky Mountains and moving eastward toward the Great Lakes, and storms moving north-eastward along the eastern coast of North America, called "extra-tropical cyclones" (Grise et al., 2013, Plante et al., 2015). The second type of storms generate oscillations on both currents and sea surface elevation (e.g. Bobanović et al., 2006, Thiebaut and Vennell, 2010, Han et al., 2012) which can induce flooding and damages (Mercer et al., 2002). Currents during or after storm passages on the Grand Banks and the surrounding regions exhibit different features. These currents can be directly induced by the storm, with strong currents starting during or just after the storm. Current oscillations can then appear after the storm occurrence and take on characteristics of topographic and inertia-gravity waves (the inertial period is about 17 h at the SPM latitude) and low-frequency currents (Tang et al., 1998).

On the Nova Scotian and Newfoundland shelves, oscillations with periods of 1-2 days have frequently been observed after storm events. The properties of these oscillations appear to depend on the duration, strength and trajectories of storms (Schwing, 1992b). One difficulty is to assess the effect of local wind and remote wind forcings (Schwing, 1992b). These oscillations are sub-inertial (i.e. their periods are larger than the inertial period) and have the characteristics of continental shelf waves propagating south-westward (e.g. Thiebaut and Vennell, 2010, Han et al., 2012). Phase velocities of these CSWs vary from ~10 -11 m s^{-1} over the Newfoundland Shelf (Tang et al., 1998, Han et al., 2012) to ~13-17 m s^{-1} over the Scotian Shelf (e.g. Tang et al., 1998, Sheng et al., 2006, Thiebaut and Vennell, 2010).

Current and temperature measurements conducted in Fortune Bay, east of SPM, during the September 1984 stratified period revealed bottom currents showing 2-3 day oscillations, related to deep water exchanges generated by the wind (White and Hay, 1994). According to these authors, two possibilities can exist : The 2-3 day wind is directly exciting a "natural modal response" on the currents at the same periods, or the wind induces upwelling/downwelling along the coast, generating bottom trapped waves.

In this paper, we present new high-frequency observations of coastal currents and sea level around SPM (at Stations A1 and A2, filled black circles, Fig. 1b). These observations were made during winter and early spring 2014 using two acoustic Doppler current profilers (ADCPs). They revealed oscillations with periods of about 2-4 days that were occasionally larger than tidal currents. They generally appeared with strong local winds and sometimes also persisted during less windy periods. The goal of this paper is to combine these observations and additional tidal gauges data with the results from a numerical model to investigate the dynamics of these oscillations. *In situ* observations and model configuration are presented in Sections 2 and 3, respectively. The analysis of ADCP observations is detailed in section 4, revealing a 2-4 day current oscillation. A realistic 2D simulation is analysed to examine the properties of these oscillations in Section 5. Then, idealistic simulations are performed to further

investigate the dynamics around SPM in Section 6. Finally, Section 7 holds discussion on the physical processes in our area of study.

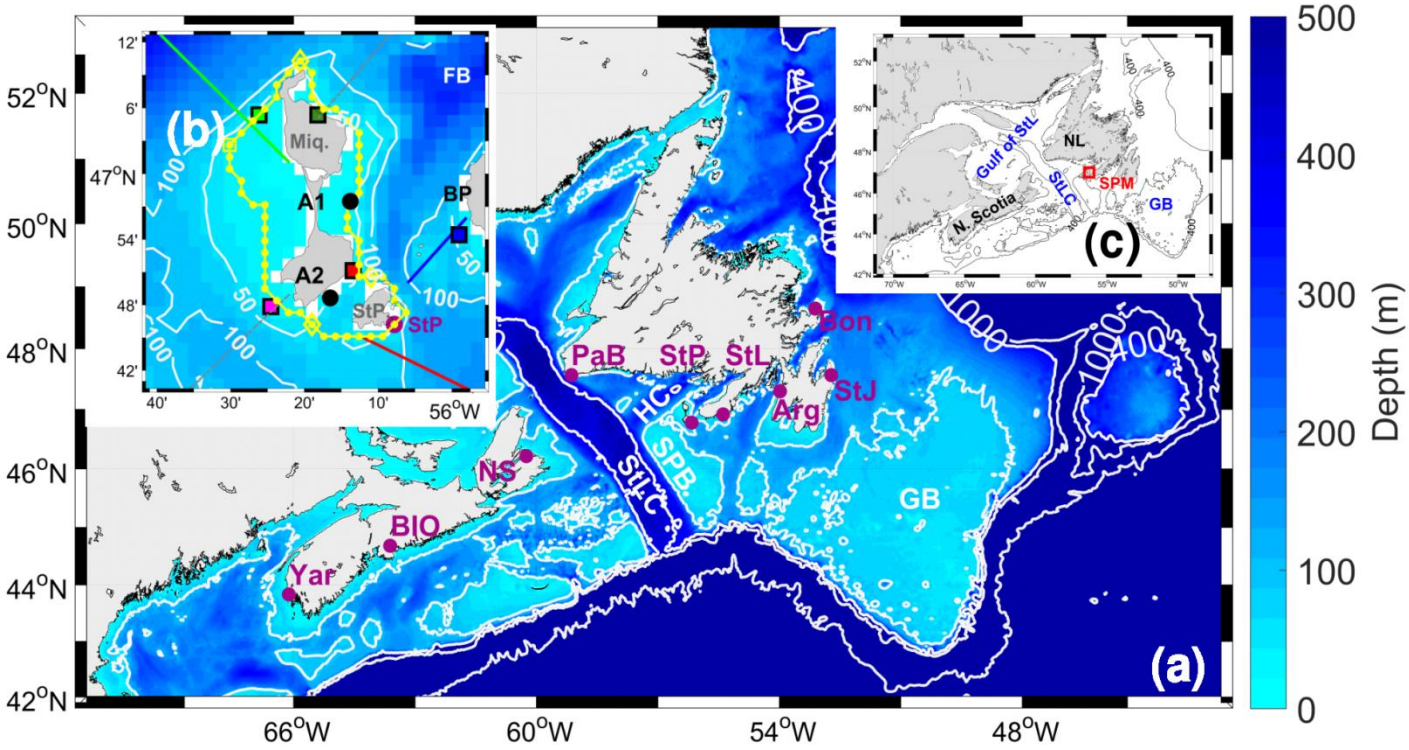

Fig. 1: Bathymetry of the modelling domain (a) with a zoom around SPM (b). In purple are locations of tide gauges used to validate the tidal components of the model: Bonavista (Bon), Saint John's (StJ), Argentia (Arg), Saint Lawrence (StL), Saint Pierre harbour (StP), Port aux Basques (PaB), North Sydney (NS), Bedford Institute of Oceanography (BIO), Yarmouth (Yar). (c) Map locating the major elements in the area such as (in blue) the Gulf of St. Lawrence (Gulf of StL), St. Lawrence Channel (StLC), the Grand Banks (GB), (in black) N.Scotia and NL (Newfoundland) Shelves and SPM archipelago (in red).

Panel b: In black: locations of the two ADCP stations A1 and A2. Lines in colour (red, blue and green) and dashed grey lines are the transects used for the Brink and Chapman (1987) programme. Filled circles with square symbols (green, blue, magenta and red) indicate areas used to investigate the schematic simulations (see Section 7). Filled yellow circles around SPM: points selected for the local-scale study indicating the perimeter of the islands along the ~30m isobath. The starting point is the open yellow square whereas diamonds delimit the segments on the perimeter of SPM (see Section 7).

Major topographic features near SPM are the Hermitage Channel (HC), Saint Pierre Bank (SPB), Fortune Bay (FB), Burin Peninsula (BP), Miquelon Island (Miq), Saint Pierre Island (StP). Bathymetry contours are plotted in white: for 50 m and 100 m (Fig. 1b), 100 m, 400 m, 1000 m and 3000 m depths (Fig. 1a).

2. Observations

2.1 Description of *in situ* measurements

In this study, the observational datasets consist of current profiles and bottom pressure measurements from ADCPs, sea level measurements from tide gauges and meteorological measurements from a weather station (wind and atmospheric pressure).

- Two ADCPs were deployed around SPM at Stations A1 and A2 (filled black circles on Fig. 1b) during winter 2014. Their characteristics are given in Table 1. The two instruments were moored at about 30 m depth for three months. To investigate the dynamics around SPM, along-shore and cross-shore current components are needed, thus requiring rotation of measured components at Station A2. For Station A1, the east (U) component was used as the cross-shore component and the north (V) component was used as the along-shore component. For Station A2, in the channel, the current velocity was projected on an SW-NE axis (with a rotation of 45°, following the orientation of the channel).

Table 1: Description of the ADCP observations.

Station	Location	Start date (dd/mm/yyyy)	End date	Water depth	Vertical sampling	Time sampling	Instrument
A1	46°57.5' N 56°13.8' W	07/03/2014	18/06/2014	28 m	1 m	10 min	RDI 600 kHz
A2	46°48.6' N 56°16.5' W	07/03/2014	22/06/2014	35 m	2 m	10 min	RDI 300 kHz

- Sea level measurements in the area were obtained from seven Canadian tidal gauge stations operated by Canada's Federal Department of Fisheries and Ocean (DFO) and from the tidal gauge station at St. Pierre harbour (StP) operated by the French Naval Oceanographic and Hydrographic Department (SHOM). Their locations are displayed in Fig 1a. The stations on Newfoundland shelf are Bonavista, St. John's, Argentia, St. Lawrence and St. Pierre harbour and Port aux Basques. The North Sydney, Bedford Institute of Oceanography and Yarmouth tidal gauges are located on the Scotian Shelf.

- Measured wind speed and direction, as well as atmospheric pressure, are available at the St. Pierre airport from the French Meteorological Service (Météo France) with a 3 hourly temporal resolution.

2.2 Data processing

- The bottom pressure measurements from the ADCP instruments were converted to sea level using the surface atmospheric pressure data from the aforementioned St. Pierre airport station assuming a constant seawater density and using

$$\zeta = \frac{P'_b - P'_a}{\overline{\rho_0} g} \quad (1)$$

where: $\overline{\rho_0}$ is the mean density of the water column, P'_b is the bottom pressure anomaly computed from the bottom pressure time series by subtracting the time-averaged value, P'_a is the atmospheric pressure anomaly computed from the surface atmospheric pressure using the same method, and g is the gravitational acceleration.

- Throughout this study, wind stress was computed according to the following equation:

$$\tau_x = Cda.u.\sqrt{u^2+v^2} \; and \; \tau_y = Cda.v.\sqrt{u^2+v^2} \quad (2)$$

where u,v are the wind speed components at 10 m (positive eastward and northward, respectively) in m s^{-1} and the wind drag coefficient Cda = 0.0016 (Muller et al., 2014).

The filtering method used to isolate the 2-4 day oscillations and to filter out the tide is a 5th order Butterworth bandpass filter (Matlab software). This filter cuts off the signal at the frequencies corresponding to periods shorter than 1.5 and longer than 5 days. The resulting time series are hereafter referred to as "filtered data".

2.3 Data analysis methods

2.3.1 Wind events definition

We isolated four strong wind events in this study, and the criterion is the peak wind stress modulus reaching 0.5 Nm^{-2} with 0.06 Nm^{-2} defining the start and end of the events.

2.3.2 Periodicities analysis

To study the periodicities in the entire times series two methods have been used. A spectral analysis has been done on the different time series with a degree of freedom equal to one. Hamming windows was used with a 50% overlap. Confidence intervals were calculated using a chi-square variable analysis.

In order to better highlight this periodicity, a second method was performed: a wavelet analysis. This method enables an analysis of a signal in time and in frequency. It makes possible to visualise intermittent periodicities. Another function has been used, the cross-wavelet analysis. It allows to identify the frequency or periodicities common to two time series. In this study, the wavelet

toolbox (Matlab) developed by (Grinsted et al. 2004) has been used. The Morlet wavelet was used for all diagnostics. The wavelet is normalized by the variance of the time series.

3. Model

3.1 Model configuration, forcing and simulation strategy

A 2D configuration of the MARS model (Lazure and Dumas, 2008) was used in our study region. The model solves the primitive equations under classical Boussinesq and hydrostatic pressure hypotheses. The modelling domain (Fig. 1a) extends from 42°N to 53°N and from 42°W to 72°W, with a spatial resolution of ~2 km (1092 x 605 horizontal Arakawa C meshes).

Open tidal boundary conditions were provided by the finite element solution (FES) 2004 (Lyard et al., 2006) with 14 tidal constituents. An ECMWF reanalysis (Owens and Hewson, 2018) was used for realistic meteorological forcing with a spatial resolution of 0.5° (~50 km) and a temporal resolution of 6 h. The forcing variables used for the realistic simulation were atmospheric pressure at sea level and wind stress computed from wind velocity at 10 m (see Eq. 2). The horizontal viscosity and the quadratic bottom friction coefficient used for the model were 6.25 m^2s^{-1} and $2.5.10^{-3}$, respectively. Temperature and salinity fields were kept constant and equal to 10°C and 32 psu ($\overline{\rho_0} \sim 1.025$), respectively. A list of the various simulations is detailed in Appendix A (Table A1). The main simulations were as follows:

- A realistic run (run A see appendix A Table A1) extending from January to June 2014 with a spin-up period of one month.
- 23 schematic simulations forced with a spatially constant wind stress field, varying sinusoidally in time (Eq. 3) to assess the influence of a periodic wind forcing and investigate the resonant behaviour of the dynamics in the SPM region.

$$\tau_{x,y} = \tau_0 sin\left(\frac{2\pi}{T}t\right), \text{with } \tau_0 = 0.25\ Nm^{-2}, and\ the\ period\ T = [1.5, 5]\ days \quad (3)$$

The amplitude of 0.25 Nm^{-2} corresponds to a wind speed of ~10 m s^{-1}. The wind stress direction was along a NE-SW axis. The parameter that was modified in these schematic simulations was the wind stress forcing period, ranging from 1.5 to 5 days. These schematic simulations were extended for 2.5 months, with the last month of all runs being used for analysis.

- Four other one-month schematic simulations with a spatially constant strong wind speed of ~20 m s^{-1}, blowing for 7 days on an ocean initially at rest from the four cardinal (N, W, S, E) directions that suddenly stopped. These simulations aimed at describing the oscillations arising during the relaxation process.

In all the schematic simulations, tidal forcing was not taken into account.

3.2 Tidal model validation

The modelled tide was validated by computing the harmonic components O1, K1, M2, and S2 of the simulated sea levels using T_TIDE (Pawlowicz et al., 2002) over the March to June 2014 period and comparing these values with the observed sea level harmonic components over the same period.

To estimate the efficiency of the model to reproduce the tide, we computed a percentage based on modelled and observed amplitude for each tidal component (in Table B1), as follows:

$$Amplitude\ error(\%) = \overline{\left(\frac{|modelled\ amplitude - observed\ amplitude|}{observed\ amplitude}\right) * 100}$$

$$phase\ error\ (°) = \overline{|modelled\ phase - observed\ phase|}$$

where the average was taken over all harbour stations and was computed for each tidal component.

The results of the harmonic analysis are detailed in Appendix Table B1 (for sea levels) and Table B2 (for current velocities).

The following average percentages were computed for all tide gauges at the different harbours. The amplitude of the semi-diurnal tidal components (respectively M2 and S2) were overestimated by 9.0% and 6.0%. Their phases were underestimated by 3.0° and 5.7° on average. The model also overestimated the diurnal tidal component (O1 and K1) amplitudes by 9.2% and 8.4%, respectively. It underestimated the phase of O1 by 5.1° and overestimated the phase of K1 by 6.35°. The simulated tidal amplitudes and phases for the sea level were thus consistent with the observations.

To validate simulated tidal currents, we compared the characteristics of the current ellipses for each tidal component from the model and from the two ADCP measurements (Table B2). The model underestimated the major axis of M2 by 24% (bias of 2.2 cms^{-1}) at A1 and 11% (bias of 0.5 cms^{-1}) at A2. The comparison between model and observations for the S2 component could reach 41.1% of error but the amplitude of the current for this component is less than 2 cms^{-1} (Table B2). The model overestimated the O1 amplitude by 42.5% (bias of 1.7 cms^{-1}) at A1 and underestimated 8.9% (bias of 0.9 cms^{-1}) at A2 station. The model underestimated the K1 amplitude by 11.9% (bias of 0.5 cms^{-1}) at A1 and 9.9% (bias of 0.7 cms^{-1}) at A2 stations. The order of magnitude for these tidal components given by the model results was consistent with observations. However the model depth at the location of A1 was ~40 m, but for the A2 location the depth was ~60 m due to a coarse grid (which is deeper than the 30 m depth of observations).

The validation of lower frequencies (~2-4 days) wind forced oscillations will be given below.

4. Results and analysis of the observations

4.1 Current data time series

The modulus of the wind stress observed at the St. Pierre airport and the current components (at the A1 and A2 stations) are given in Fig. 2. The vertical structure of the along-shore current at A1 is shown (Fig. 2e) from 10 to 26 m depth (near-surface and the near-bottom cells were blanked out). This vertical structure appeared to be nearly homogeneous. At Station A2, the current velocities also had nearly homogeneous structure over depths from 8 to 32 m (not shown). To confirm the visual assessment of the vertical structure of the currents, the standard deviations of the vertical distribution of the currents were computed at each time step (for each station and each component) and then averaged over time. The currents were normalised by the maximum value of the current over depth and through time to obtain a percentage. For A1 (A2) stations, the normalised averaged standard deviation were respectively ~6.5 % (~5.8%), ~5.7 % (~3.7 %) and ~3.6% (~3.6%) for the along-shore, cross-shore components of the current and the current speed. Thus, currents can be considered homogeneous over depth during this period. Depth-averaged cross-shore values for the A1 (A2) moorings ranged from -0.28 (-0.41) to 0.29 (0.58) m s^{-1} respectively (Fig. 2b). The depth-averaged along-shore components ranged from -0.46 (-0.49) to 0.40 (0.69) m s^{-1}.

On the wind stress modulus (Fig. 2a), two periods were distinguishable: March-April 2014 with strong winds and May-June 2014 with lighter winds. The current response (Fig. 2b, 2c) seems mostly related to wind forcing as suggested by the visual relationship between the wind stress modulus (Fig. 2a) and the along-shore current components (Fig. 2b). In March-April 2014, four events with strong wind stress moduli greater than 0.5 Nm^{-2} were identified. These wind events will be referred to below as the (13-15/03), (26-29/03), (30/03-04/04) and (8-9/04) events, respectively.

Based on the wind stress modulus values, the second event (26-29/03) was the strongest with a double peak on the wind stress modulus and indeed induced strong currents (Fig. 2b, 2c). The third event (30/03-04/04) was the longest (5 days).

The dominant signal in the sea level measurements appears to be semi-diurnal tide (Fig. 2d). The dominant periodicity of the depth-averaged current time series (Fig. 2b, c) was more difficult to define visually.

In addition to the strong events defined above, it is interesting to examine less intense wind events that occur in April and May (period of lighter winds). These events are identified by arrows (Fig. 2a) and they will be referred as medium events. They occurred on the (19-20/04), (25-26/04), (29-30/04) and (10-11/05).

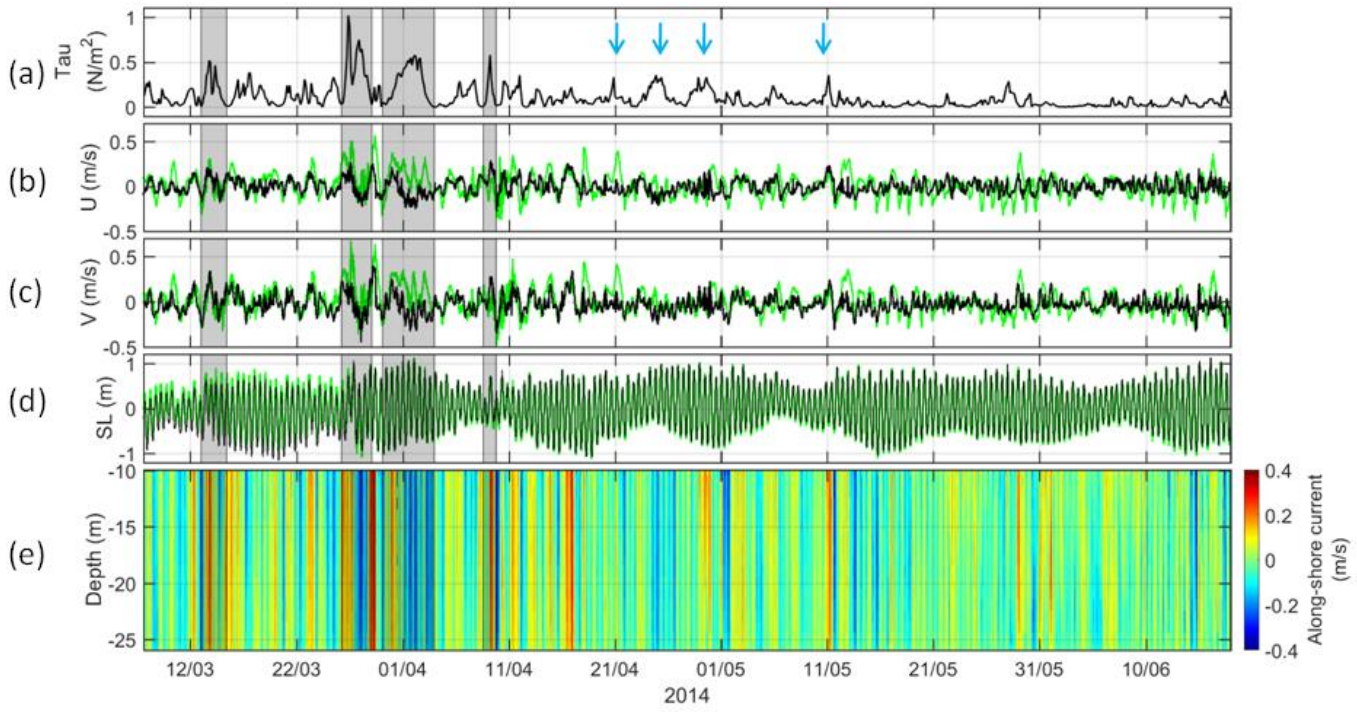

Fig. 2: (a) Computed wind stress moduli from the measurements at the St. Pierre Airport station. (b) Depth-averaged cross-shore current velocity (U) from ADCP measurements (see locations in Fig 1b), at Station A1 (black line) and Station A2 (green line). (c) Depth-averaged along-shore current velocity (V) (same colours as 2b). (d) Sea level (SL) measured by the ADCPs (same colours as 2b). (e) Time evolution of the vertical profiles of the along-shore current at the A1 station. Four strong wind events were identified (shaded grey areas, see text). The arrows point four other medium wind events mentioned in the text.

4.2 Periodicities in the measurements

A spectral analysis of the time series was conducted (not shown), but the results were not conclusive especially for the periods corresponding to the weather band (periods from 2 to 10 days). This ambiguity can be attributed to the presence of transitory phenomena and the clear lack of stationarity. Wavelet analyses were thus performed on the along-shore currents at A1 and A2 (Fig. 3a and 3b), the sea level (Fig. 3c) and the wind stress modulus computed from observations (Fig. 3d) at A2. Only sea level results at A1 are shown in Fig. 3c because the sea level analysis at A2 gave similar results.

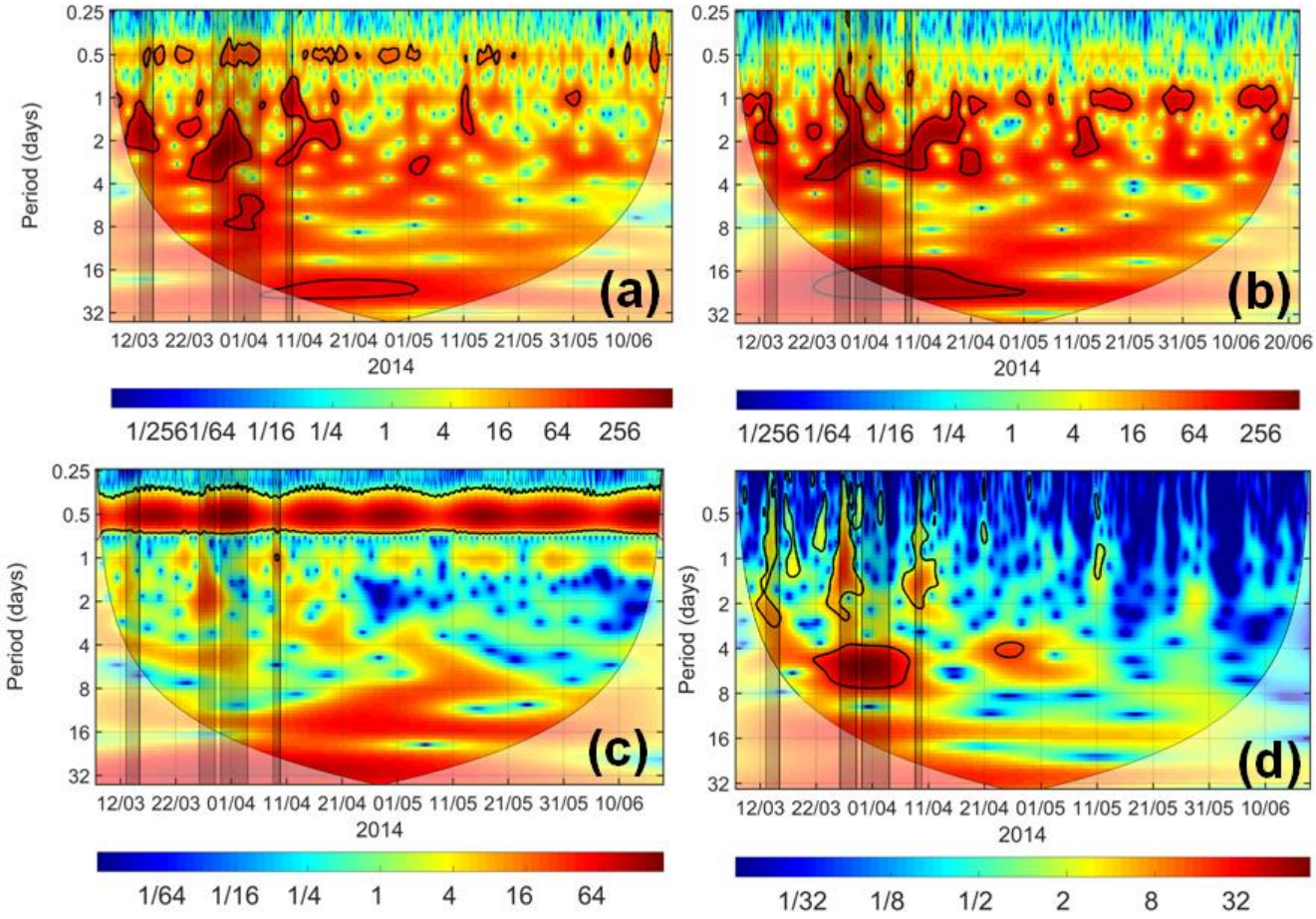

Fig. 3: Normalised power wavelet density of the depth-averaged along-shore current at the A1 station (a), at the A2 station (b), (c) the sea level at the A1 location, (d) the wind stress modulus computed from observations at St. Pierre Airport. On all panels, the areas enclosed by the black contour lines indicate the periods with significance above 95%. The four strong wind events were identified (shaded grey areas).

The normalised power wavelet density plots showed significant periods (using a 95% significance criterion) for the along-shore current at both ADCP locations (Fig. 3a, 3b) ranging from 1.5 to 4 days. During the first strong event (13-15/03), the main periodicity of the along-shore current was between 1 and 2 days. The second strong event (26-29/03) and the third strong event (30/03-04/04) induced oscillations of the along-shore current with a periodicity of between 1.5 to 4 days. On the wavelet diagram of the along-shore current at A1 (Fig. 3a), a dominant periodicity of between 4 to 8 days was observed for the third event (30/03-04/04). These large periods cannot be seen on the wavelet diagram of the along-shore current at A2 (Fig. 3b). The last strong wind event (8-9/04) had an oscillatory signature on along-shore current with periods of between 1.5 and 3 days at Station A1 (Fig. 3a) and at Station A2 (Fig. 3b). On the wavelet of the wind stress modulus, the strong events had periodicities of up to 2 to 3 days (Fig. 3d) with the exception of the third event which had only a periodicity of 4 to 8 days .

Regarding the sea level (Fig. 3c), a 1-2 day period appeared during the second event (26-29/03). This signature was not found in the 95% significance level (black contour lines, Fig. 3c), but can be noted as an influence of the wind on the sea level.

The short medium events of (19-20/04) and (10-11/05) are visible on the wavelet diagram of the wind stress modulus (Fig. 3d) with periods around 1 day. These wind events can also be seen on along-shore current wavelet diagrams (Fig. 3a, 3b) with a periodicity of 1 to 2 days (except the (19-20/04) event at A1 station). Conversely, the two longer medium events in April are visible on the wind stress modulus at periods around 4 days (Fig. 3d) but they have no signature on the along-shore currents (at both stations Fig. 3a, 3b). This will be discussed later (section 7).

4.3 Relationship between the wind and the current

The along-shore currents thus appeared to be linked to wind stress forcing. To better identify the relationship between the wind and the along-shore current, a cross-wavelet analysis (Grinsted et al., 2004) was performed between the wind stress modulus and current at the A1 (Fig. 4a) and A2 (Fig. 4b) stations. The along-shore components of the wind stress were computed at each ADCP station.

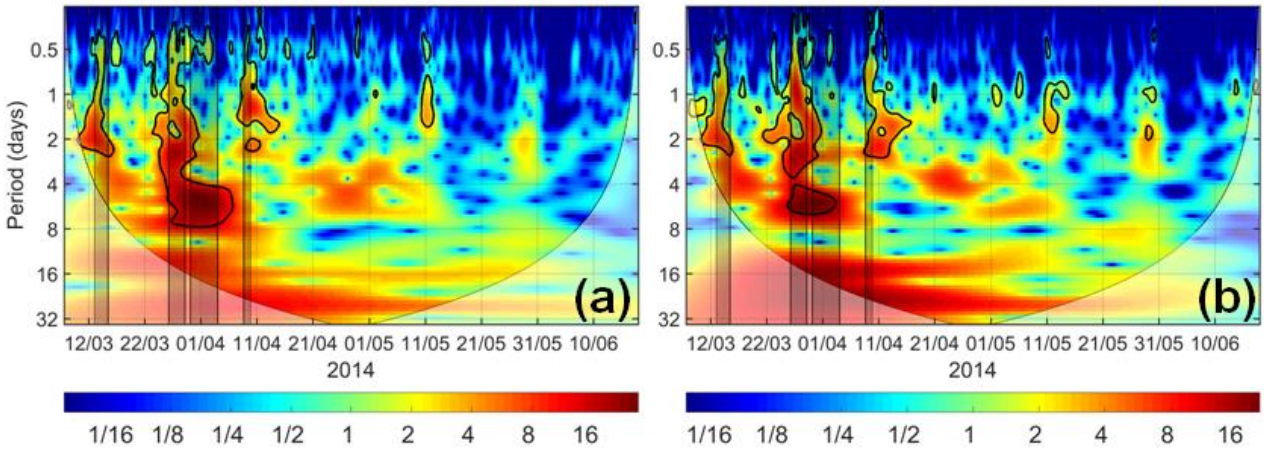

Fig. 4: Cross wavelet analysis between the wind stress modulus (computed from the St. Pierre Airport station measurements) and along-shore current at the A1 station (a) and the A2 station (b). On all panels, the areas enclosed by the black contour lines indicate the periods with significance greater than 95%. The four strong wind events are identified (shaded grey areas).

The wind stress modulus and along-shore currents at A1 (Fig. 4a) and A2 (Fig. 4b) were highly correlated, especially during strong wind events. There were several common periods for the along-shore wind stress and along-shore current at the A1 and A2 stations: ~0.5 to ~4 days for the first (13-15/03) and last events (8-9/04). At the A1 station for the second (26-29/03) event, the common periods for the along-shore wind stress and along-shore current were between 0.5 and 8 days (Fig. 4a, Fig. 4b). For the third event (30/03-04/04) the periodicity in common between the wind stress and the along-shore current is form 4 to 8 days. There is also a high-power cross-wavelet density for three other meteorological events, on (8-10/03), (24-26/03) and (10-11/05).

4.4 Storm characteristics

The tracks of storms affecting the area of study are given in Fig. 5, by plotting the location of the minimum atmospheric pressure extracted from ECMWF data (Owens and Hewson, 2018) during the period from March to May 2014. Only the main wind events are shown, among which the four strong wind events outlined in Fig. 2, with wind velocities higher than 17 m s^{-1} at SPM (Table 2). Two examples of storms which induced weaker wind velocities at SPM (between 13.4 and 14.9 m s^{-1}, see Table 2) were added (dashed lines on Fig. 5). The 8-10/03 and 24-26/03 events (in Fig. 5 green and magenta dashed lines) occurred just before the strong events (Fig. 2) respectively the 13-15/03 and 26-29/03 (in Fig. 5 green and magenta solid lines). The four last storms (shown by the arrows Fig. 2a) are represented with dash lines (Fig. 5).

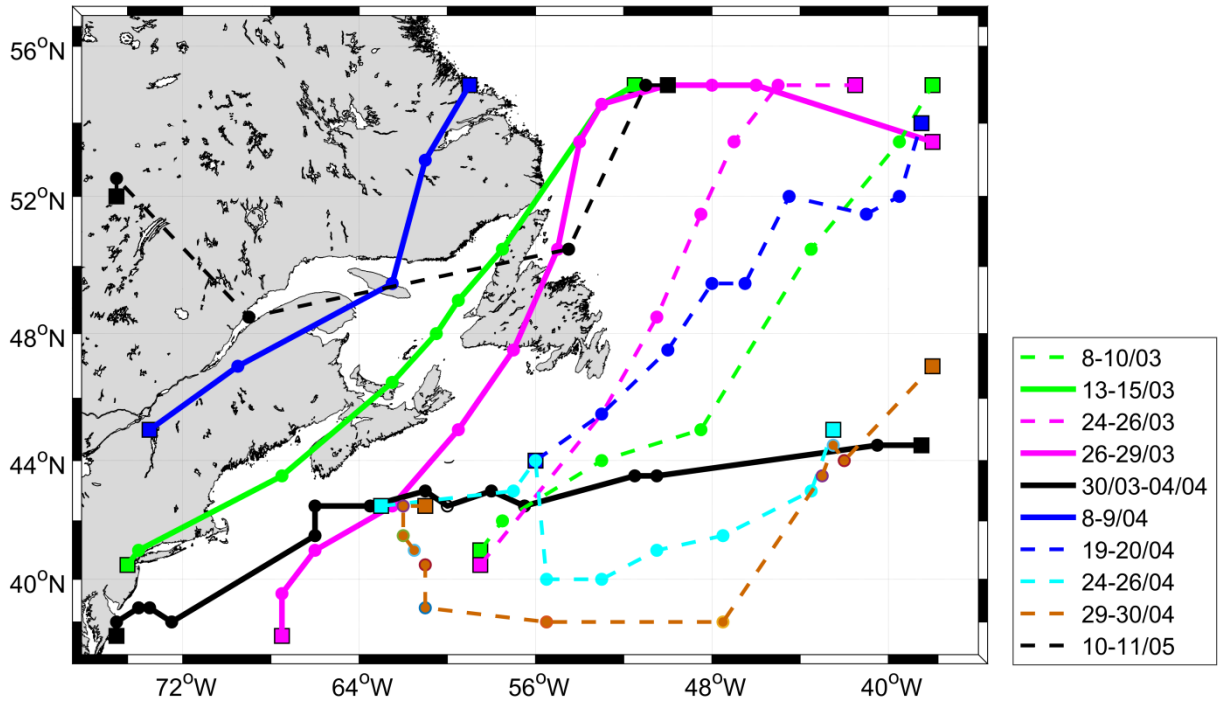

Fig. 5: Trajectories of storms in the area, during the March to June 2014 period, computed from the position of the pressure field minima over the domain presented in Fig. 1, and from the ECMWF dataset. The four strong wind events near SPM are indicated with thick lines. The dashed lines represent storm tracks with weaker wind stress maxima at the SPM location.

Table 2: Characteristics of each wind event presented in Fig. 5. The minimum pressure and maximum wind speed were calculated by taking the minimum of the pressure field and maximum of wind velocity field over the domain presented in Fig. 5 and for the period of each event. The storm displacement speed is estimated over the duration of the storm. The wind speed and atmospheric pressure fields are from the ECMWF reanalysed dataset.

Wind events	8-10/03	13-15/03	24-26/03	26-29/03	30/03-04/04	8-9/04	19-20/04	24-26/04	29-30/04	10-11/05
Maximum wind velocities at SPM (m s^{-1})	13.4	18.0	14.4	25.2	19.0	19.0	14.4	14.9	14.4	14.9
Maximum wind velocities over Fig. 5 domain (m s^{-1})	24.9	21.9	25.3	31.7	20.8	25.3	27.2	21.0	19.2	17.8
Minimum pressure over Fig. 5 domain (in hPa)	966.4	977.8	962.4	951.7	987.6	978.0	967.4	983.2	991.8	993.2
Estimated storm mean displacement speed (m s^{-1})	**18.4**	**13.5**	**17.6**	**12.8**	**10.1**	**17.5**	**9.5**	**9.6**	**10.5**	**15.5**

The four strong wind events (thick lines, Fig. 5) that have a strong signature on the local wind stress modulus (Fig. 2a) were meteorological depression events with maximum wind velocities between ~18 and ~32 m s^{-1} and pressure field reaching a minimum of between ~952 and ~993 hPa (Table 2). According to the storm tracks, nearly all of them were "extra-tropical cyclones" (Grise et al., 2013), originating in the south-west and moving north-eastward, roughly in the along-coast direction for this region. The third strong event (30/03-04/04) (thick black line) was a 5 day event (Fig. 2a) with an eastward moving direction. It was also one of the slowest moving event (Table 2). For the 13-15/03 event (green line on Fig. 5), the wavelet density diagrams

(Fig. 3a, 3b) show strong current oscillations around 2 days period. However, the oscillations started earlier, and may have been induced by the previous storm, the 8-10/03 event (dashed green line, Fig. 5) which crossed the region a few days earlier. For the 8-10/03 event, the wind stress was weaker than for other events (~0.2 Nm^{-2}, Fig. 2). The same interpretation can be made for the 24-26/03 (dashed magenta line, Fig. 5) and 26-29/03 (solid magenta line, Fig. 5) events.

The two medium events in April (24-26/04) and (29-30/04) were long in term of duration they moved in the same direction as the third strong event (30/03-04/04), from west to east.

5 Analysis of the numerical model results

5.1 Realistic simulation

The simulation used in this section takes into account the tidal and meteorological forcings (Table A1, simulation A). The filtered along-shore currents and sea level data from the realistic simulation and observations are shown in Fig. 6b, 6c and 6d. Filtering the observations removes the majority of tidal forcing. We compared the along-shore current components, on which the impact of the wind is expected to be the strongest (Csanady, 1981).

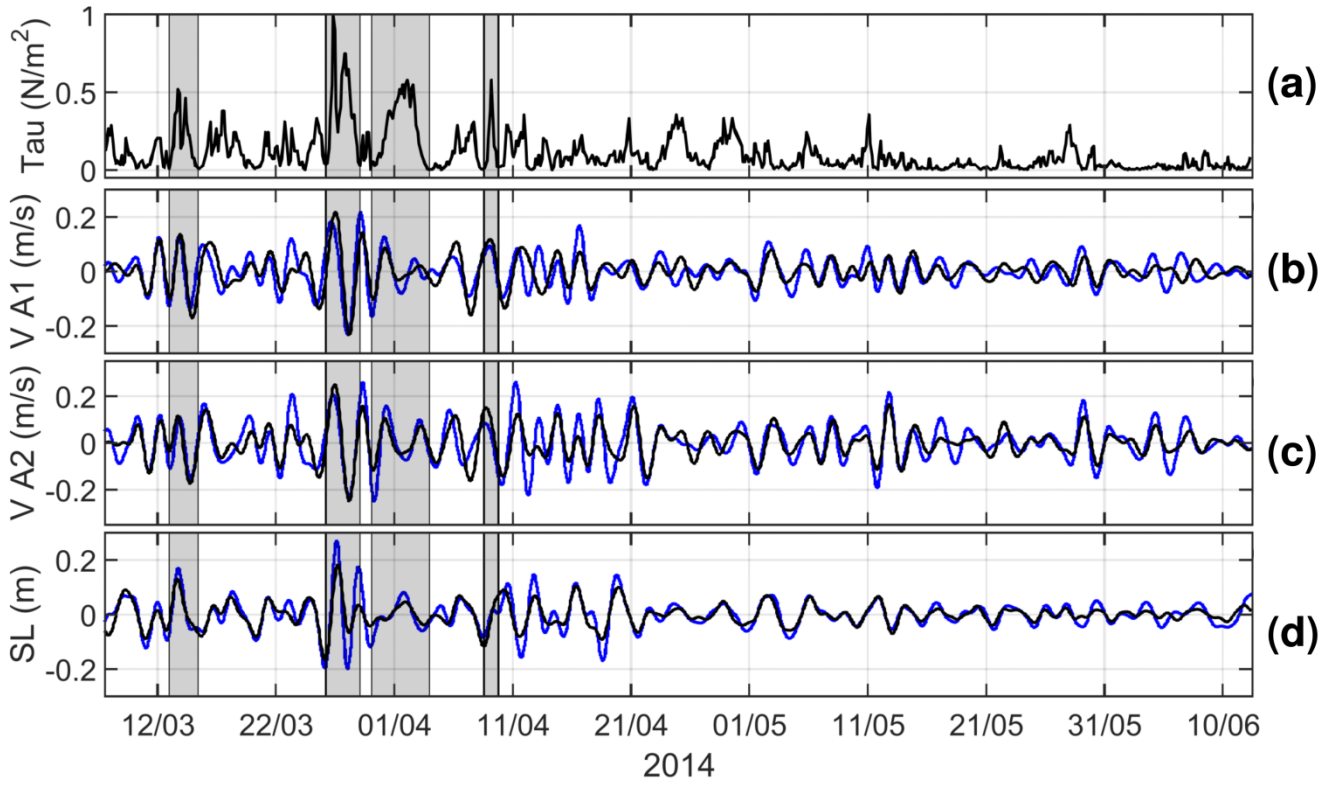

Fig. 6: (a) Wind stress modulus at the Saint Pierre airport. Filtered along-shore current velocity (V), at the A1 station (b) and at the A2 station (c). (d) Filtered sea level at A1. The blue curve corresponds to observations and the black curve corresponds to the simulation results from the realistic run.

The results from the model, in Fig. 6b, 6c and 6d, appeared in fairly good agreement with observed along-shore currents at both stations and with sea level observations. The model slight underestimated the along-shore current, especially at A2 (Fig. 6c). The oscillations were consistently strong on both of the along-shore current and the sea level from 26/03 to 26/04. Fig. 6c also shows that the timing of the wind events (shaded grey areas) coincided with greater sea level amplitude. This will be discussed in greater detail in Section 7.2.

For better quantification and validation, the root mean square error (RMSE) and the Willmott score (Willmott, 1981) were computed (Eq. 4) as in (Ma et al., 2015):

$$\mathrm{RMSE} = \sqrt{\frac{\sum(\mathrm{MOD}-\mathrm{OBS})^2}{\mathrm{N}}} \qquad WS = 1 - \frac{\sum(MOD-OBS)^2}{\sum[|MOD-\overline{OBS}|+|OBS-\overline{OBS}|]^2} \tag{4}$$

where MOD refers to the filtered model results, OBS and $\overline{OBS}$ refer to the filtered and time-averaged filtered observations, respectively, for the along-shore current and sea level at the A1 and A2 stations. N refers to the number of values for both observed and modelled time series. If WS is equal to 1, the model results agree with the data perfectly.

Table 3: Root mean square error (RMSE) and the Willmott score (WS), computed using (Eq. 4) for the filtered along-shore currents and sea levels at A1 and A2.

	RMSE			**WS (**Willmott score)		
	Entire time series	March-April	May-June	Entire time series	March-April	May-June
Filtered along-shore current at A1	4.6 cm/s	5.2 cm/s	3.6 cm/s	0.82	0.84	0.73
Filtered along-shore current at A2	5.2 cm/s	6.0 cm/s	3.9 cm/s	0.88	0.88	0.89
Filtered sea level at A1	2.8 cm	3.5 cm	1.5 cm	0.92	0.91	0.94
Filtered sea level at A2	3.6 cm	4.5 cm	1.8 cm	0.88	0.87	0.91

The RMSE of the filtered along-shore currents at the two ADCP stations was between 3.6 and 6.0 cm/s. For the filtered sea level, the RMSE was between 1.5 and 4.5 cm. The WS values were between 0.73 and 0.89 for the along-shore current. The weakest WS score (0.73) corresponds to the last period (May-June) at Station A1 (Fig. 6b). The WS score also showed high values for the sea level (0.87 to 0.94). Based on Fig. 6 and in Table 3, the model correctly captured the wind-induced low-frequency dynamics around SPM.

To verify that meteorological forcings are the main cause of the generation of these oscillations, another simulation was performed for the March-June 2014 period with meteorological forcing only (i.e. no tide, Table A1 simulation B). The modelled 2-4 day oscillations were also qualitatively in good agreement with the observations (not shown). In this case, the amplitude of the oscillations was overestimated for the along-shore currents and the sea level. The WS scores were between 0.53 and 0.80 for the along-shore current and between 0.82 and 0.87 for the sea level. According to these criteria, this simulation was less realistic. The overestimation of the 2-4 day oscillations may be due to the absence of enhanced bottom friction produced by tides.

5.2 Spatialisation of the 2-4 day oscillations

To estimate the spatial distribution of the 2-4 day oscillations, we computed the time-average of the filtered current speed (Eq. 5) over the whole domain. This computation was done for the period from 26/03 to 26/04 including the four strong meteorological depressions described above and giving rise to strong 2-4 day current oscillations.

$$Filtered\ current\ speed\ = \left(\sqrt{U(t)_{filtered}{}^2 + V(t)_{filtered}{}^2}\right) \quad (5)$$

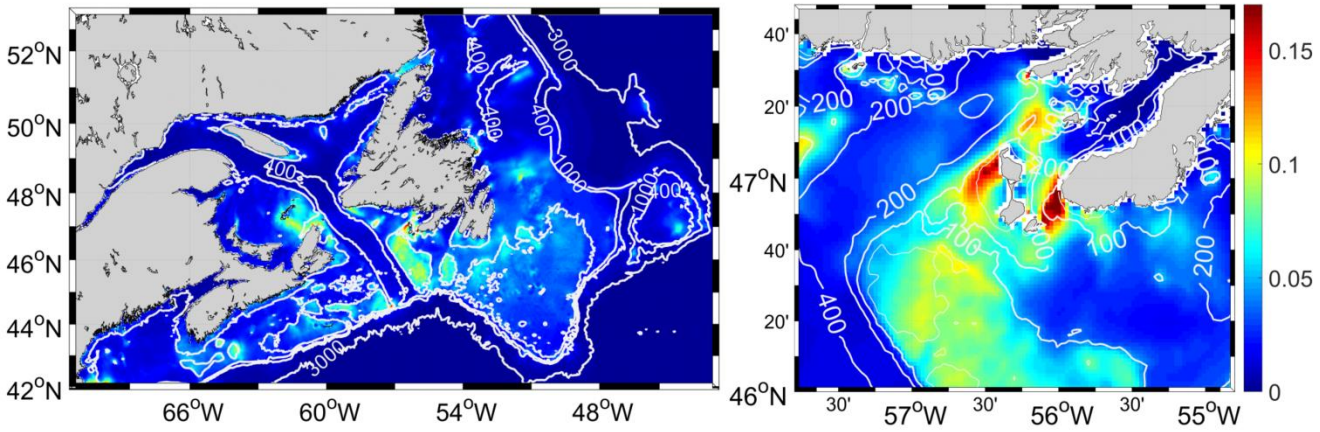

Fig. 7: Map of the time average of filtered current speed field from the realistic simulation (right panel) for the domain and (left panel) zoom of SPM region. The averaging period covers 26/03/2014 to 26/04/2014. White lines show the bathymetry contours: at 50 m, 100 m, 200 m 400 m (right panel), 100 m, 400 m, 1000 m and 3000 m (left panel) depths.

The largest averaged filtered speeds were found around SPM and St. Pierre Bank and in the Gulf of Saint Lawrence (Fig. 7). Some local maxima were also found over the Grand Banks and the Scotian shelf. The highest values of the mean velocity of the filtered current speed were found around SPM islands and reached 0.17 m s^{-1}. They were localised and amplified north-west of SPM and near Burin Peninsula. There was another maximum further north of SPM, reaching 0.12 m s^{-1}. On St. Pierre Bank (Fig. 7, right panel), the mean of the velocity of the filtered current speed ranged from 0.05 to 0.11m s^{-1}.

6 Schematic simulations

6.1 Results for oscillating wind forcing

To investigate the response of the coastal ocean to various periods of forcing, we performed 23 simulations with a spatially homogeneous, but periodic sinusoidal wind (Table A1, simulations E[1:23]). For simplicity, the tide was not taken into account in these simulations. Wind stress fields were oriented north-eastward – south-westward (Eq. 3) with a period varying from 1.5 to 5 days.

The response to this wind forcing was investigated at six stations around the SPM archipelago: Stations A1 and A2 and four additional points distributed around the archipelago (coloured squares in Fig. 1b) at 30 m depth. The response to sinusoidal wind stress was a sinusoidal current of the same period and with harmonics of lower amplitude (not shown). At each point, we calculated the time-averaged (during the last 10 periods of each simulation) current speed.

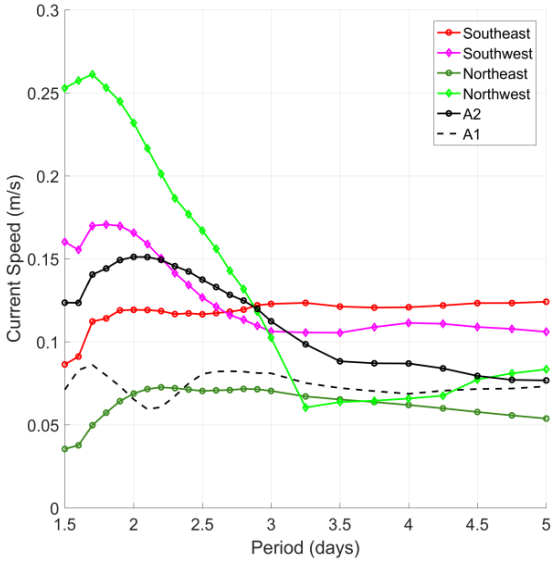

Fig. 8: Time-averaged current speed (over the last 10 periods of each simulation) taken at six locations around the SPM archipelago, red: south-east of SPM, magenta: south-west of SPM, dark green: north-east of SPM, light green: north-west of SPM, black: A2 location, dashed black line: A1.

Fig. 8 shows the amplification of the current velocities around the period of 2 days (from 1.7 to 2.4 days). For the north-west and south-west locations, current speeds reached their maxima at periods ~1.7 days and decreased rapidly for longer periods. Maximum amplification (0.27 m/s) was obtained at the north-west location for a 1.7 day period. At the A2 station, the strongest current was reached for a period around 2 days, decreased for periods between 2-3 days and remained stable for longer periods. Along the eastern side of Miquelon Island (north-east, south-east and A1 stations) the strongest currents reached their maximum at periods of between 1.7 and 2.8 days (two maxima are observed at A1 station). Currents were generally weaker on the eastern side than the western side.

To visualise the spatial distribution of current forced by spatially homogeneous periodic winds, the average current speed of the last 10 periods of each simulation (Fig. 9) was calculated. The energy fluxes were computed for the same period (LeBlond and Mysak, 1981)

$$\overrightarrow{Flux} = \left(\overline{\rho_0 g(H+\zeta)\zeta u}^{10periods},\ \overline{\rho_0 g(H+\zeta)\zeta v}^{10periods} \right) \quad (6)$$

where ρ_0, g are the water density and the gravitational acceleration, respectively, H is the sea floor depth, ζ, u, v are the sea level and the two components of the current velocity, respectively, and ($\overline{\ }^{10periods}$) is the average over the last 10 periods of each simulation.

These variables are shown for wind stress with a periodicity of 1.7 days (Fig. 9a), 2 days (Fig.9b), 2.4 days (Fig. 9c), 3 days (Fig. 9d).

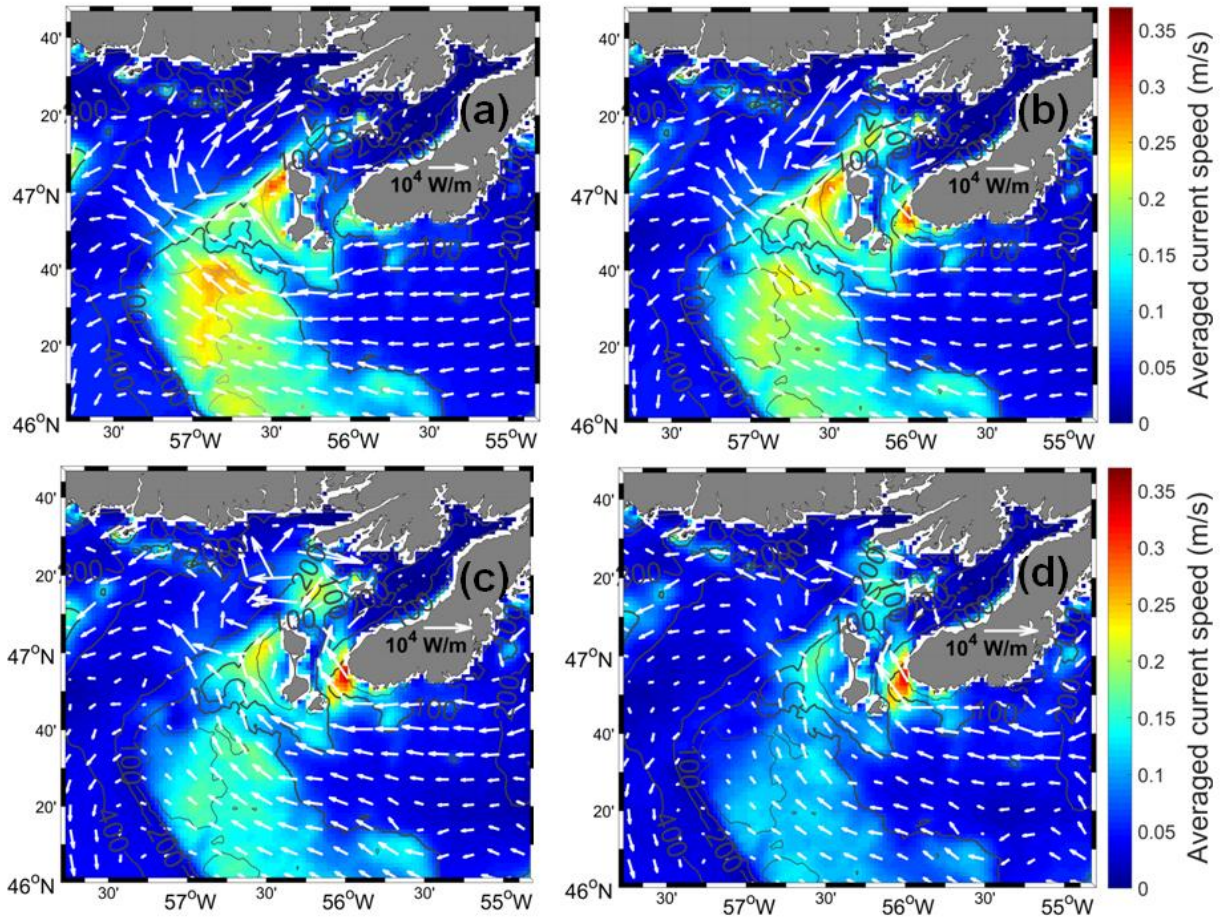

Fig. 9: Maps of the averaged current speed and energy fluxes (white arrows) computed for the last 10 periods of each simulation. Simulation with a 1.7-day period (a), 2-day period (b), 2.4-day period (c), 3-day period (d).

The averaged current speed was maximal in SPM and St. Pierre Bank areas. The spatial pattern appeared to be very similar to the result of the realistic simulation (Fig. 7). For a 1.7-day wind period (Fig. 9a), the largest values of the averaged current speed were located northwest of SPM, near Burin Peninsula and on the north-eastern part of St. Pierre Bank. From Fig. 9a to Fig. 9d the averaged current speed around SPM decayed with longer periods. Conversely, near Burin Peninsula, another current speed maximum appeared. It reached ~0.37 m s^{-1} for a wind periodicity of 2.4 days (Fig. 9c) and decreased slightly for 3-day period wind stress (Fig. 9d).

The energy fluxes (Fig. 9) were oriented westward south of Burin Peninsula. West of SPM and over the St. Pierre Bank, they were oriented north-westward and seemed to decrease with increasing periods. Conversely, between SPM and Burin Peninsula, the northward fluxes increased with increasing period and reached their maxima for periods of 2.4 and 3 days (Fig. 9c, d).

The same numerical experiment was performed using the same periodic wind stress, but for the perpendicular direction (NW-SE). This experiment exhibited weaker currents, but very similar spatial patterns (not shown).

6.2 Free oscillations resulting from relaxation

Four simulations were performed with a wind blowing for 7 days at a speed of 20 m s^{-1} from all four cardinal directions (N, S, E, W). Fig. 10 a shows the along-shore current (calculated after a 45° rotation of the axes) spectrum, taken north-west of SPM (filled green circle, Fig. 1b) for the four wind directions. Fig. 10b represents the entire time series of the along-shore current taken at the same location. The spectral analysis was done for a period of 10 days, immediately after the storm. Fig. 10c and 10d show the spectrum and the time series of the along-shore current, respectively, at a location near Burin Peninsula (blue square, Fig. 1b).

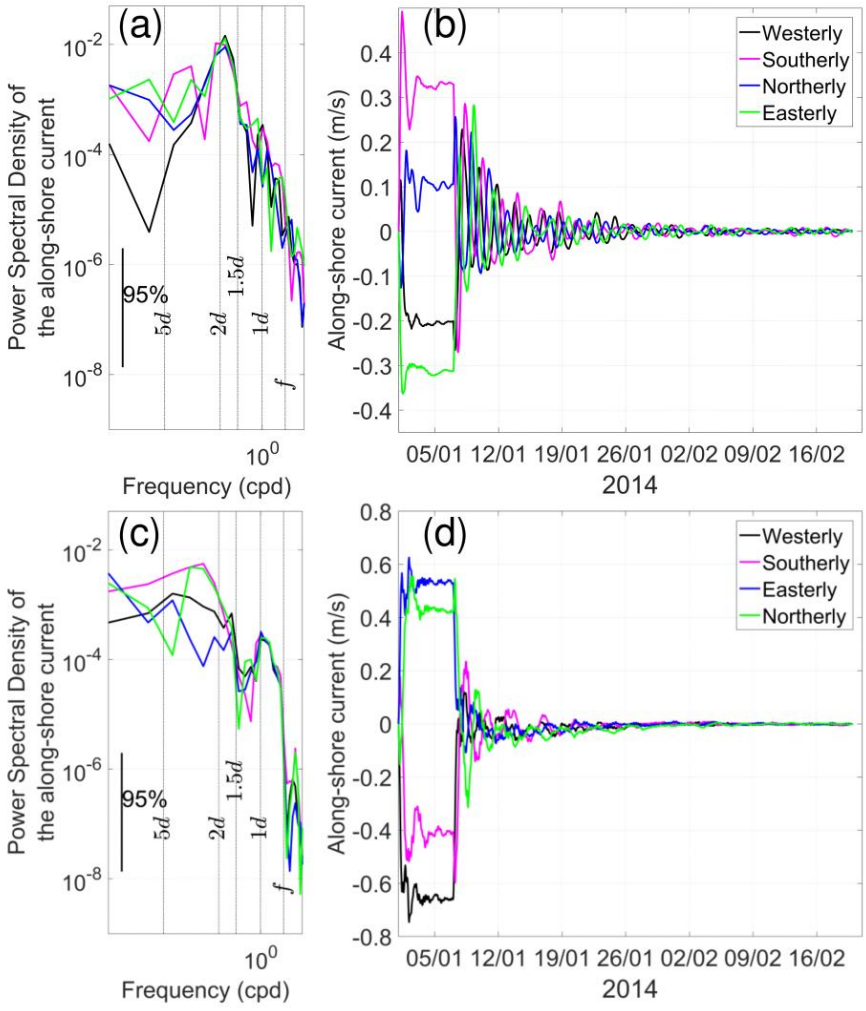

Fig. 10: Spectrum of the along-shore current taken north-west of SPM (a) (green square in Fig. 1b) and near Burin Peninsula (c) (blue square in Fig. 1b). Time series of the along-shore currents, at the location north-west SPM (b) and near Burin Peninsula (d). Westerly (in black), southerly (in magenta), easterly (in blue), northerly (in green) winds.

When the wind stops, the along-shore current oscillates and its amplitude decreases exponentially (Fig. 10 b and Fig. 10 d) under dissipation effects. To reduce the amplitude of the current by ~50% the system needs around three days.

Fig. 10a shows that for a wind blowing from each cardinal direction, the along-shore current maxima northwest of SPM were obtained for a period of about 1.7 days (1.7 to 2 days). Near Burin Peninsula (Fig. 10c), the amplitude of the along-shore current is larger than the amplitude north-west of Miquelon (Fig. 10a). The dominant periods were also larger, between 2.6 and 4.3 days.

The other observation sites (blue, red, magenta and the two ADCP stations in Fig. 1b) were investigated with the same analysis (not shown). The periodicity of the along-shore component of the current in response to the four types of wind (blowing from each cardinal direction) was also between 1.5 and 5 days.

The amplitude of the along-shore current response close to the SPM coast was stronger at the north-western location (Fig. 10a), but it remained weaker than near Burin Peninsula (Fig. 10c), which is consistent with the sinusoidal wind experiment results (Fig. 8).

7 Discussion

During winter and spring 2014, barotropic 2-4 day current oscillations were observed, especially during and after strong wind events and they can be an order of magnitude greater than tidal currents for a few days (Fig. 2). Their periodicities extended from 1.5 to 5 days, but were maximal in the range 2-4 days according to the wavelet analysis (Fig. 3). There is a strong correlation between along-shore currents and wind stress at these periodicities (Fig. 4). Currents and wind stress are triggered by regional-scale meteorological events crossing through the area of study (Fig. 5). These 2-4 day current oscillations were correctly modelled around SPM in winter 2014 (Fig. 6 and Table 3). They were strongly amplified around SPM islands, as shown by the modelled large time-averaged barotropic current speed (Fig. 7). The current speed in the SPM area was enhanced at wind stress periods of 1.7 to 2.4 days (Fig. 8). The averaged current speed from schematic simulations with a periodic wind showed a spatial pattern similar to the realistic simulation with two maxima: one north-west of SPM for periods of 1.7-2 days and the other near Burin Peninsula for periods of 2.4-3 days (Fig. 9). Energy fluxes mostly came from the east and increased around SPM (Fig. 9). The wind relaxation simulations were in line with periodic forcing simulations and suggest preferential along-shore current periods of around 1.7-2 days north-west of SPM and between 1.5 and 5 days near Burin Peninsula in response to a strong wind event (Fig. 10).

7.1 Low-frequency sea levels at the regional scale

To investigate the effect of these 2-4 day oscillations at the regional scale, the observed and modelled sea levels at different tide gauges along the Newfoundland coast (in purple in Fig. 1a) are shown in Fig. 11. The inverse barometer effect is taken into account in this analysis to remove the direct influence of the surface atmospheric pressure on the seal level (e.g. Han, 2012, Ma, 2015). Without this correction the sea level is at first order rise under a depression and drop under high pressure (~1 hPa = 1 cm). These sea levels were filtered to eliminate the tides.

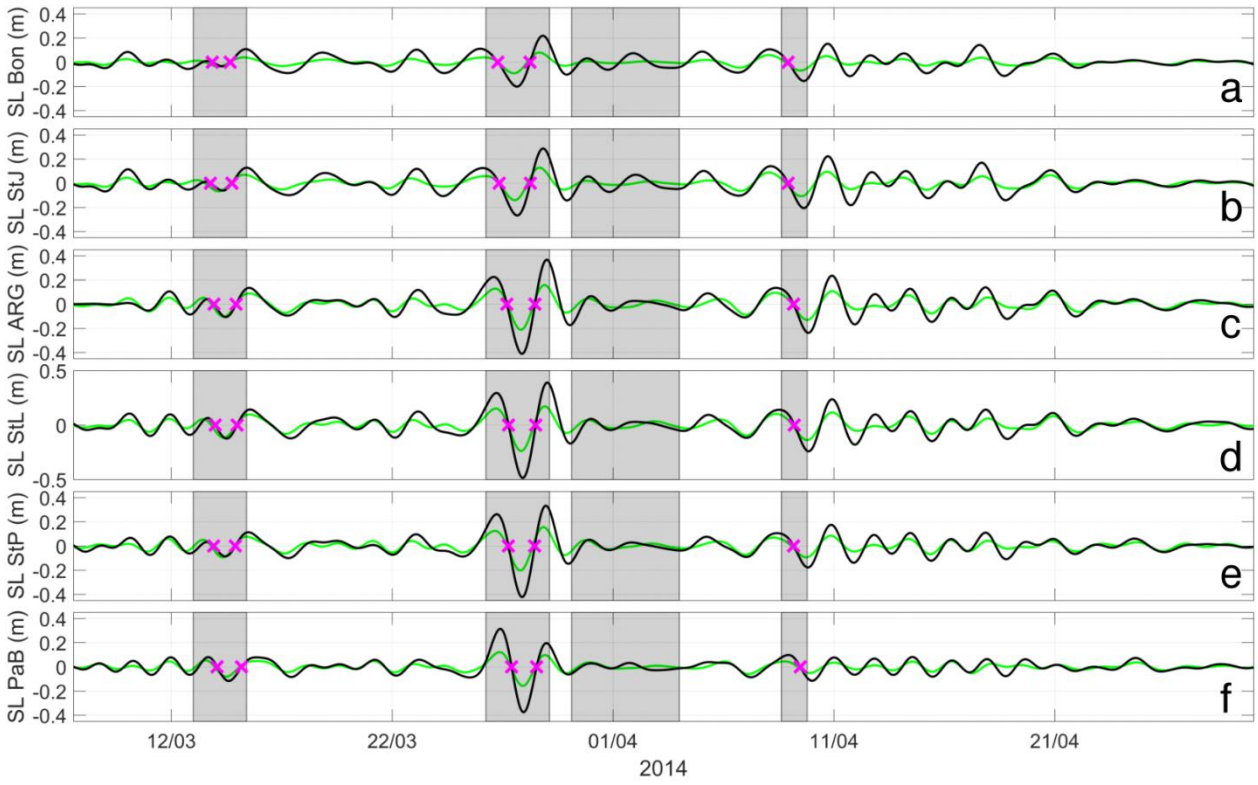

Fig. 11: Filtered sea level from the observations (black curves) and from the model (green curves) during wind events from 09/03 to 20/04 at the Bonavista (a), St. John's (b), Argentia (c), Saint Lawrence (d), St. Pierre (e) and Port aux Basques (f) stations. These time series were corrected for the inverse barometer effect and detided (filtered between 1.5 to 5 days). The location of the zero crossing tracked (see text) were highlighted by a magenta cross.

The 2-4 day oscillations left a signature on the filtered sea level measured by the gauges (Fig. 11). They can reach an amplitude of ~0.20-0.25 m (at Bonavista, St. John's and Port aux Basques) and 0.5 m at St Lawrence. The model underestimated the oscillations, with an RMSE between 4.5 and 6.5 cm and a Willmott score between 0.74 and 0.86.

On Fig. 11, an equatorward (southwestward) propagation can be seen for the sea levels from the harbours (Bonavista, St. John's, Argentia, St. Lawrence, St. Pierre, Port aux Basques). We tracked the propagation of these oscillations during three of the strong events (magenta cross Fig. 11). The third event had not been analysed because it did not induce significant oscillations. We identified five zero crossing points and we plotted the time of arrival at each tide gauge stations for the first event (Fig. 12a), second event (Fig.12b) and fourth event (Fig. 12c). The equatorward propagation is obvious in the model and the observations.

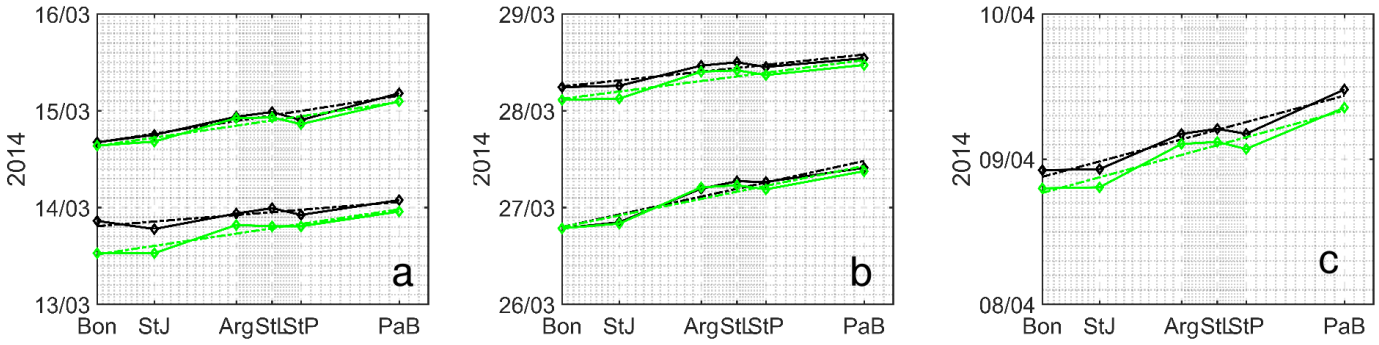

Fig. 12: Propagation of the zero crossing points (magenta crosses on Fig. 11) for the different tide gauges stations (Bon, StJ, Arg, StL, StP, PaB). In black, the observations, in green, the data form modelling results. Dash-dotted lines are representing the linear regression of the selected point at each stations for a zero crossing.

By doing a linear regression for each zero crossing point followed at each station (Fig. 12), we computed the velocity of propagation for the observations and the model (Table 4) by using distance 1 between tide gauges stations (see appendix C table C1, the distance between Bonavista and Port aux Basques is ~730 km). Except for the first event, simulations and observations are in good agreement.

The first strong event oscillation had a very low amplitude at Bonavista and Saint John's tide gauge stations that the model did not reproduce accurately. It is having an impact on our velocity estimation and explaining the difference between observation and simulation. The averaged velocity was about 20.9 ms^{-1} for the observations and 17.2 ms^{-1} for the model.

More generally, we noticed a amplification of the oscillations for the tide gauges located west of Saint John's.

Table 4: Velocity estimation (using distance 1 between tide gauges stations see appendix C table C1) for three of the four strong events.

Velocity of propagation	First event 1	First event 2	Second event 1	Second event 2	Fourth event
From the observations	33.8	17.5	12.4	25.6	15.1
From the model	18.1	18.6	13.4	21.1	14.9

We made a second estimate of the phase velocity using lagged correlations on filtered sea levels (Fig. 11) from 09/03 to 20/04. The phase velocities had been calculated using different distances between the gauges by either assuming a straight line between each bay extremities and harbours (distance 1 detailed in appendix C in Table C1 and Fig. C3) or estimating the along-shore distance if the wave is propagating into the bays (distance 2 detailed in appendix C in Table C1 and Fig. C4).

Table 5: Estimation of the phase velocity (V_φ) and correlation coefficient (Corr) from a lag correlation of sea level. For each harbour, 'Obs' is the estimation of the phase velocity based on observations and 'Mod' for modelling results. In parentheses, the phase velocity was estimated with the distance following the coast. Both distance 1 and distance 2 following the coast are presented in Appendix C Table C.1. The positive values indicate a south-westward propagation.

Harbour data		St. John's		Argentia		St. Lawrence		St. Pierre		Port aux Basques	
		V_φ (ms^{-1})	Corr	V_φ (ms^{-1})	Corr	V_φ ($m\ s^{-1}$)	Corr	V_φ ($m\ s^{-1}$)	Corr	V_φ ($m\ s^{-1}$)	Corr
Bonavista	Obs	46.1 (47.9)	0.98	18.1 (20.6)	0.91	19.6 (23.6)	0.89	27.3 (31.9)	0.82	24.3 (33.3)	0.67
	Mod	76.8 (79.9)	0.98	13.3 (15.2)	0.92	16.0 (19.3)	0.91	22.8 (23.2)	0.87	19.9 (27.3)	0.76
St. John's	Obs			12.2 (14.8)	0.93	15.3 (19.7)	0.92	23.6 (28.7)	0.83	22.4 (32.4)	0.69
	Mod			8.9 (10.8)	0.94	12.2 (15.7)	0.93	19.0 (23.2)	0.89	17.9 (25.9)	0.77
Argentia	Obs					28.8 (42.5)	0.98	Infinite (lag=0 h)	0.93	38.5 (74.2)	0.85
	Mod					72.0 (106.2)	0.99	-43.3 (-53.3)	0.98	40.9 (58.3)	0.90
St. Lawrence	Obs							-29 (-26.9)	0.94	46.5 (74.2)	0.89
	Mod							-14.5 (-13.4)	0.98	36.5 (58.3)	0.91
St. Pierre	Obs									30.4 (54.5)	0.86
	Mod									19.8 (35.5)	0.94

The phase velocities values ranged between ~12 and ~48 m s^{-1} for the observations and between ~9 and ~ 80 m s^{-1} for the model results in the area (Table 5). Observations and model estimations of phase velocities appeared to be generally consistent. In Table

5, the phase velocities between Bonavista and St. John's were unrealistically large, 46 m s^{-1} or 79 m s^{-1}. Owing that the sampling interval of our records is 10 min and the distance between the two harbours is short (about 60 km), the phase velocity between St. Lawrence and St. Pierre is difficult to estimate. The phase velocity had unrealistically large values between Argentia and St. Lawrence, Argentia and St. Pierre, and Argentia and Port aux Basques. Therefore, in the following analysis, we did not consider the measurements in Argentia. Its location deep inside the bay may cause local effects that blur the ~2-4 day oscillations.

By taking into account the realistic values (less than ~30 m s^{-1}) of the phase velocity estimation (Table 5), the averaged phase velocities become (respectively for distance 1 - distance 2) ~21.5 - ~28.8 m s^{-1} for the observations and ~16.6 - ~21.8 m s^{-1} for the model. The final phase velocity range we considered for this study was ~16.6 - ~28.8 m s^{-1} (this corresponds to the minimum value given by the model and the maximum value given by the observations, on average, in Table 5). Other studies use small portions of tide gauge records (2-3 days to 10 days), during post-storm surge periods (Han et al., 2012, Ma et al., 2015, Thiebaut and Vennell, 2010). In our study, the analysis was conducted over a period of time that included four episodes of strong winds. The result is an average correlation and lag for the total analysed period (9/03 - 20/04).

Previous studies give estimated values of phase velocities of between 10-17 m s^{-1} (Tang et al., 1998, Sheng et al., 2006, Thiebaut and Vennell, 2010, Han et al., 2012, Ma et al., 2015). In Ma et al. (2015), the authors observed a phase velocity of around 20 m s^{-1} for a frequency of around 0.7 cpd. Our results show a wave with a 2-4 day period, with a phase velocity averaging between 16.6 - ~28.8 m s^{-1}.

The previously cited authors have interpreted these sea level oscillations as the manifestation of CSWs propagating south-westward. Our 2-4 day oscillations may thus be interpreted as the first mode of a CSW propagating on the Newfoundland Shelf with the coast on its right and referred to as the 'regional CSW'.

7.2 At the local scale

7.2.1 Sea level anomalies and transport field

To better understand the circulation due to the 2-4 day oscillations at the 'local' scale, around SPM, we computed the time evolution of the sea level anomalies and transports around SPM from the realistic simulation (with wind and tidal forcings) during the second strong wind event (26-29/03). Sea level anomalies were estimated from the filtered modelled sea levels. Specifically, we computed the spatial sea level anomaly (ζ' in Eq. 7) using

$$\zeta'_{(x,y,t)} = \zeta(x,y,t)_{filtered} - \overline{\zeta(x,y,t)_{filtered}}^{x,y} \quad (7)$$

At each time step and at each point of the model, the spatial average $\left(\overline{\zeta(x,y,t)_{filtered}}^{x,y}\right)$ was computed over neighbouring points (selected within a circle of a given radius). Then, at each point and time step, this spatial average was subtracted from the sea level given by the model $\left(\zeta(x,y,t)_{filtered}\right)$. This process creates a sea level filtered spatially, as in (Cyr et al., 2016), equal to the sea level anomaly to filter out the large-scale motions and to underline local-scale motions. We used a radius of 50 km to compute the sea level average. The same computation was done with different radii (for example 20 km and 80 km) with similar results.

The transport field (H(x,y).$\vec{u}(x,y,t)$) was computed from the simulated current velocities (1.5 - 5 day filtered).

The snapshots (Fig. 13) start from the first time the filtered sea level reached zero at St. Pierre after the beginning of the (26-29/03) event (Fig. 13a) until the beginning of the third wind event (30/03 at 16h, 96 hours later) with an interval of 12 h.

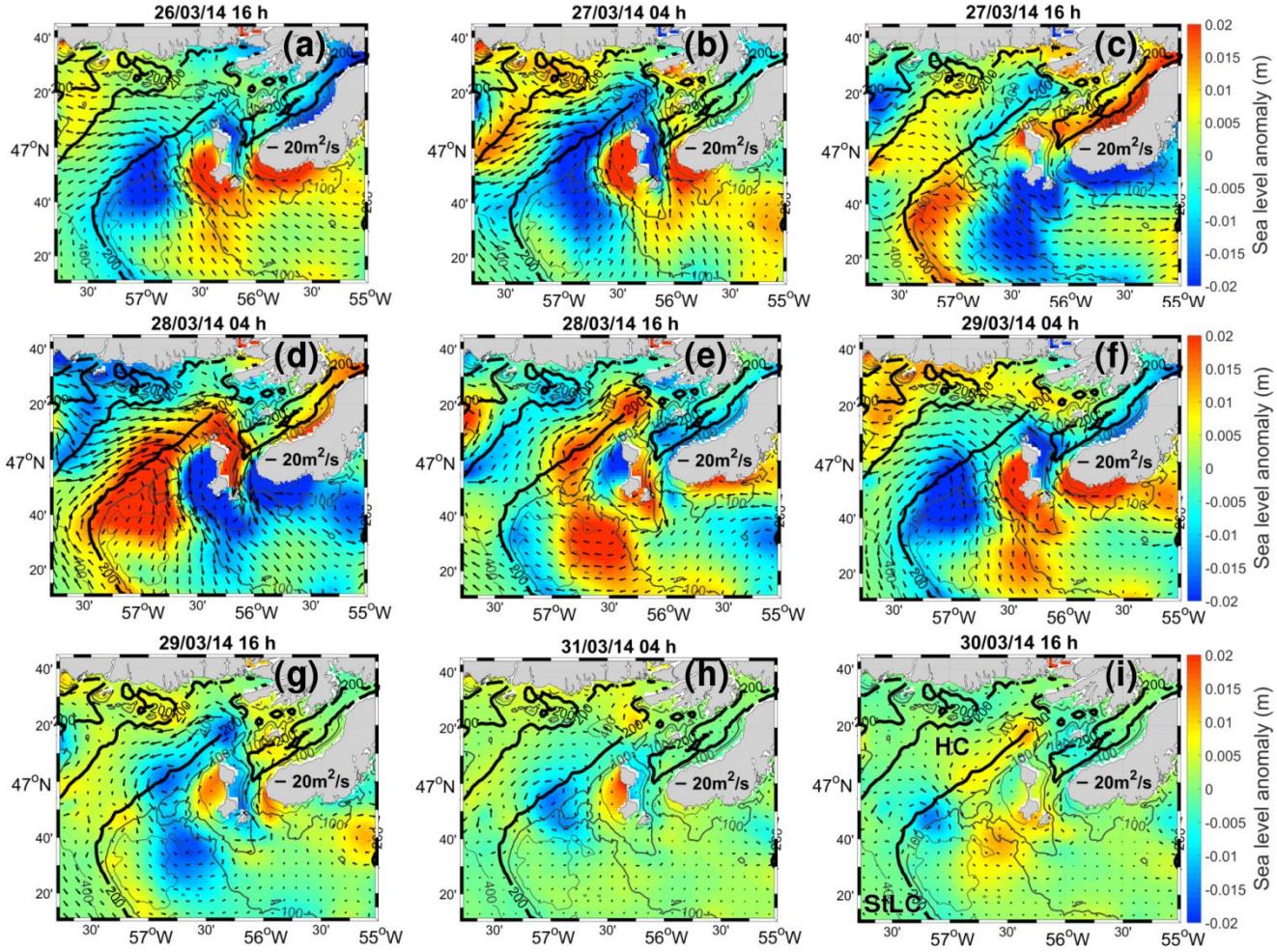

Fig. 13: Arrows: transports (H(x,y).$\vec{u}(x,y,t)$) computed from the filtered currents. Colours: sea level anomalies computed from the filtered sea levels (eq. 6) using the realistic simulation over four days, from 26/03 16h to 30/03 16h every 12h. Isobath 200 m is represented with a thick black line and on Fig 13i Hermitage and St. Lawrence channels have been identified (by HC and StLC in black).

In the first snapshot (Fig. 13a), a positive sea level anomaly (reaching ~0.03 m) is located on the south-western shelf of SPM (in depths less than 100m) with strong northward transports. A negative sea level anomaly is located on the north-eastern side of SPM also with strong northward transports. Then, 12 hours later the positive sea level anomaly had moved northward, still associated with northward transport, and the negative sea level anomaly on the eastern side had moved southward (Fig. 13b). In Fig. 13c, the positive anomaly is located north of SPM with transports flowing eastward and southward NE of Miquelon, while the negative anomaly is located south of SPM with eastward transports. The fourth snapshot (Fig. 13d) shows a pattern around SPM which is nearly the opposite of Fig. 13a, with a negative anomaly on the western side of SPM and a positive anomaly on the eastern side of SPM with southward transport on both sides of SPM. The positive anomaly on the eastern side keeps propagating southward (Fig. 13e, f) and the negative anomaly on the western side propagates northward. Fig. 13a and 13f give similar results and highlight a period of ~2.5 days. The last three snapshots (Fig. 13g, 13h, 13i) show a lower amplitude for the sea level anomalies (reaching ~0.02 m) and the transports, as the storm has moved away. The sea level anomaly and transport patterns were consistent and revealed clockwise displacements of positive and negative anomalies around SPM islands. This pattern also occurs during and after the other wind events (not shown).

There are cyclonic and anticyclonic circulations associated with negative and positive sea level anomalies along the southern slope of Hermitage Channel. A strong positive sea level anomaly with anticyclonic transport is located on the slope between Hermitage Channel and St. Pierre Bank in Fig. 13d. This positive sea level anomaly moving north-eastward tends to be separated into two cores with a distance ~ 45 km (Fig. 13e). The same pattern can be observed with negative sea level anomalies and anticyclonic transport (Fig. 13a, 13b and Fig. 13 f and 13g).

The transport field in the Hermitage Channel is on the south-westward direction at a latitude of 47°N and a longitude of 57°W (Fig. 13a, 13b, Fig. 13f). At the same time (Fig. 13a, 13b, 13f), the transport points south-eastward (along the slope) in the St. Lawrence Channel suggesting a connexion between the two channels. These transports describe the filling and emptying of the two channels.

7.2.2 Sea level anomalies at the local scale

To investigate these 2-4 day oscillations at the local scale and assess their phase velocities, a time-distance diagram was plotted with the sea level anomalies given by (Eq. 7) along the perimeter of the ~30 m depth isobath around SPM islands (Fig. 14).

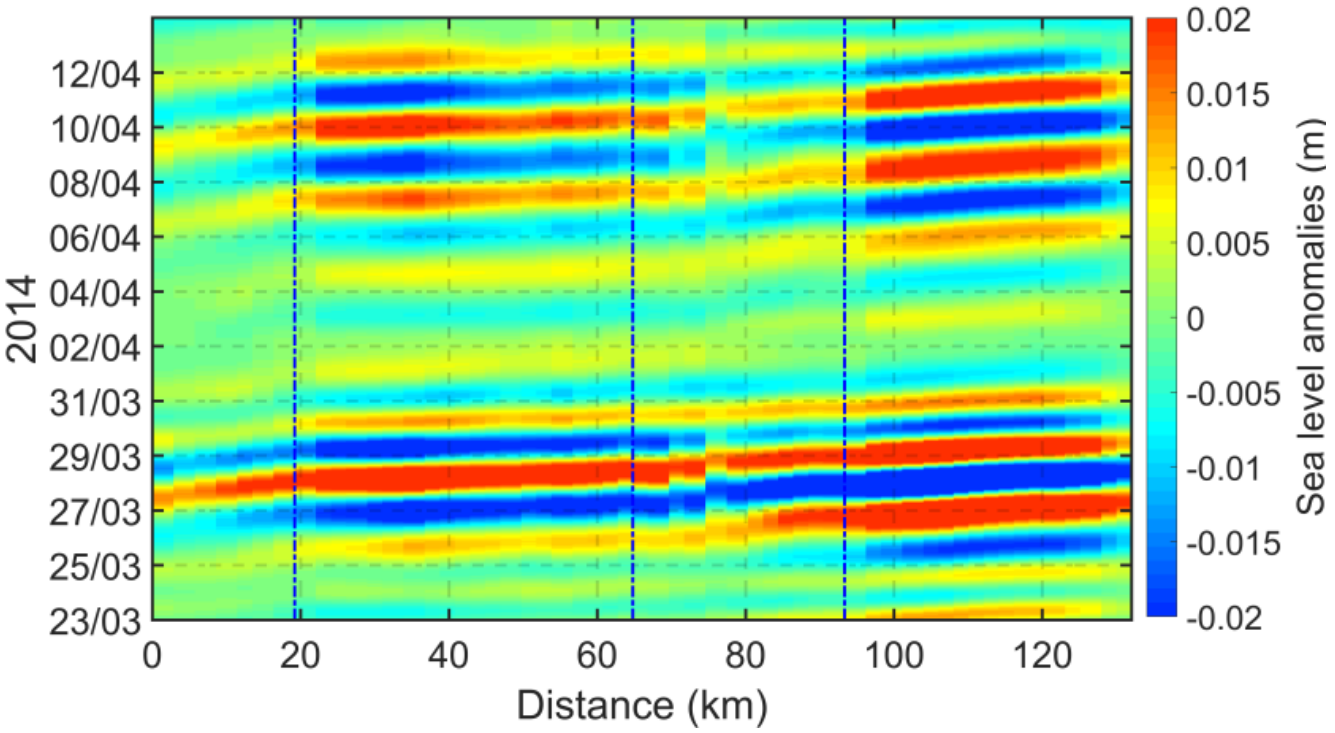

Fig. 14: Time-distance diagram along ~30 m isobath. The points selected are represented in Fig. 1 by filled yellow circles. The blue dashed lines represent four segments between diamond points in Fig. 1. The first segment is north-west of SPM (from the square to the first diamond in Fig. 1b) The second segment corresponds to the eastern side of SPM from the northern tip to the entrance of the channel ("La Baie") between the two SPM islands (between first and second diamond in Fig. 1b). The third segment is the segment east and south of St. Pierre island (between second and third diamond on Fig. 1b). The last segment is on the western side of SPM from the channel between the two SPM islands to the western point of the isobaths (between third and fourth diamond in Fig. 1b).

The period plotted is from 23/03 to 15/04 and includes the 26-29/03, 30/03-4/04 and 8-9/04 wind events. The slopes made by the successive positive and negative sea level anomalies are positive and indicate a clockwise propagation around SPM. The 26-29/03 wind event and the 8-9/04 wind event are outlined by strong sea level anomalies (reaching 0.03 m), on the second segment (eastern side of SPM) and fourth segment (western side of SPM). The oscillation induced by the 8-9/04 event persisted at least until 12/04 probably because the wind continued to blow, although less strongly (Fig. 6a).

The periodicity was evaluated by selecting the dates for which the sea level anomaly was equal to zero at the beginning (distance =0) and end (distance =130 km) of the island tour during the two events in Fig. 14 (26-29/03) and (8-9/04). On average it was ~55 h (ranging from 42-64 h, over the period shown in Fig. 14). The phase velocities were estimated, for a complete rotation around SPM, for the events for which the sea level anomaly amplitude was larger than 0.015 m (from Fig. 14). The estimate gave a phase velocity ranging from 0.53 to 0.89 m s^{-1} (on average 0.70 m s^{-1} for the period from 23/03 to 15/04) along the 30 m isobath. For each segment in Fig. 14, we obtained a phase velocity equal to ~0.3 m s^{-1} for the first segment, ~1.5 m s^{-1} for the second segment, ~0.5 m s^{-1} for the third segment and ~0.7 m s^{-1} for the last segment.

In Table 6, the phase velocities were estimated for the longest and shortest periods of oscillations observed, i.e. 42 h and 64 h. For this computation, the distances were estimated with two methods, a short perimeter that does not include St. Pierre Island and the other that includes the whole archipelago.

Table 6: Estimates of phase velocities according to the different perimeters (including or not including St. Pierre Island (StP)) for different isobaths (from 20 m to 100 m) and periodicities (from 42 h to 64 h).

Isobath	Length without StP (km)	Length with StP (km)	Phase velocity m s^{-1} (period of 42 h)	Phase velocity m s^{-1} (period of 64 h)
20 m	94	108	0.62 / 0.70	0.41 / 0.47
40 m	105	135	0.69 / 0.90	0.45 / 0.59
60 m	119	140	0.79 / 0.93	0.52 / 0.61
80 m	130	150	0.86 / 1.00	0.56 / 0.65
100 m	140	181	0.93 / 1.20	0.61 / 0.79

In Table 6, different phase velocities were computed for perimeters following different isobaths, from 20 m to 100 m depth, with the minimum and maximum periods of the oscillations. They range from 0.41 to 1.20 m s^{-1}, with an average of ~0.73 m s^{-1}.

7.2.3 Continental shelf wave at the local scale in the SPM area

The clockwise motions of the anomalies, which are localised around SPM, are suggestive of topographical trapped wave dynamics (Huthnance, 1974, Tang et al., 1998). The intensification of the sea level anomalies near the coast and the estimated phase velocity seemed consistent with the theory. To evaluate this hypothesis, the simplified model developed by (Brink and Chapman, 1987), with a barotropic assumption, was used to compute the dispersion curve of a free wave propagating around SPM.

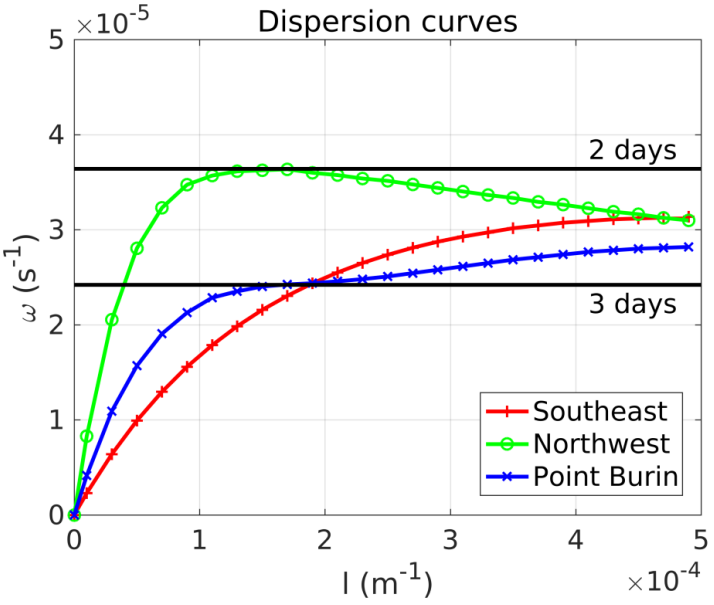

Fig. 15: Dispersion curves for the first mode of a free barotropic continental shelf wave computed with the code of Brink and Chapman (1987). Horizontal lines: 2 and 3 day periods. The three curves are for the bathymetric profiles around SPM in Fig. 1b shown in identical colours (green: north-west of Miquelon, red: the south-east profile and blue: the profile near Burin Peninsula). The transects which are represented by dashed grey lines, are not shown in this figure.

This model assumes a straight coastline and uniform along-shore bathymetry. We applied the model on five different cross-shore transects: four around SPM (north-west, north-east, south-east and south-west) and one off Burin Peninsula (see Fig. 1b). The resulting dispersion curves for mode 1 CSWs for three transects (north-west, south-east of SPM and Burin Peninsula) are

displayed in Fig. 15. Results for the north-east and south-west transects (dashed grey lines Fig. 1b) lie between north-west and south-east curves and are not shown, for clarity. Maximum phase speeds (~ 0.8 m s^{-1}) were obtained for long waves on the north-west transect. Phase speeds decreased on other transects around SPM as along-shore wavenumber (l) increased. These phase speeds were roughly in the same range as the ones observed in Fig. 14 and Table 6. Group velocity, and thus energy propagation, approached zero for l ~ 1.7 10^{-4} m^{-1} (which corresponds to a wavelength ~37 km) for the north-west and Burin Peninsula transects. This wavelength roughly corresponds to the spacing of the successive anomalies (about 42 km) observed in numerical modelling results on the slope north-west of SPM (Fig. 13e and 13g). The corresponding periods obtained with the Brink and Chapman model are respectively about 2.0 days (north-west transect) and about 3.0 days (Burin Peninsula transect). These periods are close to the periods for which the maximum response was obtained with numerical modelling (see Fig. 9) north-west of SPM (about 1.7 days) and near Burin Peninsula (about 2.4 days). Both the north-west of SPM and the Burin Peninsula areas correspond to regions of converging energy fluxes (Fig. 9). We thus believe that CSWs are involved in these local dynamics and in particular that the amplification observed (Fig. 7) north-west of the SPM archipelago and near Burin can be attributed to such processes. We shall refer to this CSW as the 'local CSW'.

7.3 Physical interpretation in terms of 'regional' and 'local' continental shelf waves

Based on previous work and using analyses of the sea levels (Fig. 11), there is evidence for a 'regional CSW' forced by wind stress with a period of about 2 to 4 days. It propagates with a large phase speed 16.6 - ~28.8 m s^{-1}, in the south-westward direction on the Newfoundland Shelf, consistent with the dispersion curves previously reported. Two dispersion curves calculated using the Brink and Chapman (1987) program, with almost similar N-S transects, extending from the Newfoundland coast to the deep ocean, give similar results (Thiebaut and Vennell 2010, their Fig. 10 and Han et al. 2012, their Fig. 6). From their dispersion curves, wavenumbers for a period of 2 days correspond to phase velocities of around 20 m s^{-1} or higher. This CSW is characterized by small wavenumbers (from 0 to 0.1 10^{-5} m^{-1}), and thus wavelengths of hundreds or thousands of km. This result is also consistent with equatorward energy fluxes (Fig. 9).

However, the wind speed is not the only factor explaining the triggering of the CSW. As shown on Fig. 2, four medium events have been pointed out (19-20/04), (25-26/04, 29-30/04) and (10-11/05). On the wavelet diagrams (Fig. 4) the two longest events (25-30/04) had no signature on the filtered sea level. The wavelet diagram of the wind stress modulus (Fig. 3d) for these events had a periodicity of ~4 days. The same conclusion can be applied on the third strong event (30/03-04/04). For this event, the criteria based on the strength of the wind stress modulus is satisfied. The wavelet analysis of the wind stress modulus (Fig. 3d) showed that the periodicities of this event were between 4-8 days. Cross-wavelet analysis (Fig. 4) suggests that the common periodicities in were also between 4-8 days but there is no signature around 2 days. This is well in line with the result of Fig. 11 which showed that the third event did not trigger 2-4 day oscillations. Conversely, the (19-20/04), (10-11/05) events had higher frequencies (~1 day). They also had a signature on the wavelet and cross-wavelet diagrams (Fig. 3 and Fig. 4). (Han, 2012) also noticed that an hurricane crossing the area in one day is able to induce ~2-4 day oscillations in St. John's and Argentia.

This 'regional CSW' would then force a 'local CSW' with clockwise propagation of positive and negative anomalies around SPM islands (Fig. 13). These propagations suggest an azimuthal mode 1 for this 'local CSW' propagating around SPM for periods of around 2 days. The estimation of phase velocity for the 'local CSW' is ~0.7 m s^{-1} with the 2D model (Fig. 14). This velocity estimation is also consistent with the result of the (Brink and Chapman, 1987) model (Fig. 15), which gave a maximum phase velocity of ~0.8 ms^{-1}. By focusing on the time distance diagram (Fig. 14), the propagation around SPM is clockwise, but the phase velocity is not constant for the entire perimeter of SPM. This inconsistency is likely due to the irregular slopes and the shape of the coastline.

The 'local CSW' dispersion curve (Fig. 15) shows a group velocity equal to zero around the 2 day period with the north-west transect. It indicates that this region may be in the 'resonant' regime (Gordon and Huthnance, 1987) for a wind stress period of

about 2 days. This is consistent with the results of the idealistic numerical experiments showing an amplification of the current speed northwest SPM for wind forcing with a period about 1.7 to 2 days (Fig. 8, 9) and the relaxation experiments that showed oscillations of similar periods (Fig. 10a).

For the two other transects on the eastern side of SPM, the group velocity drops to zero for larger periods around ~2.5 or ~3 days. This drop in velocity is consistent with observations that show correlations between wind and along-shore currents on a broader band of periods at the A1 station than at A2 (Fig. 4). However, east of SPM, this resonance was less pronounced. Thus, on the scale of the entire archipelago, a natural period around ~2-4 days seems to emerge as shown in Fig. 14.

Filtered sea level anomalies and filtered transports show an eastward propagation in the Hermitage Channel and on the northern part of St. Pierre Bank (Fig. 13). This propagation may be due to a wave propagating on the slope of the HC channel and may be another effect of the 'regional CSW' on this topographic feature.

In this region, the interactions of waves with bathymetry are difficult to estimate, especially due to large bathymetry changes. The topographic structure of the archipelago and its surroundings is complex (with the Hermitage and St. Lawrence channels, St. Pierre Bank) and can induce complicated oscillatory phenomena. It can also induce non-linear responses and interactions between modes (Hsieh and Mysak, 1980). Scattering into higher modes, reflexions, interactions between modes, evanescent waves (e.g. Wilkin and Chapman, 1987, Hsieh and Buchwald, 1985) are also likely. These phenomena complicate the dynamical responses especially due to the channels, banks and topographic features around SPM.

8 Conclusions

Wind was shown to have an important impact on the dynamics in the area of SPM in winter 2014, especially with the "extra-tropical cyclones" travelling along the North-eastern Atlantic Ocean coast. In winter and spring 2014, nearly barotropic oscillations were observed in the currents around SPM. Wavelet analyses showed that, among various phenomena, significant oscillations with a periodicity from 1.5 to 5 days occurred in wind stress and currents. The cross-wavelet analysis showed a strong correlation between along-shore current and wind stress for these periodicities and that the wind clearly triggers current oscillations.

Our numerical 2D model was able to reproduce these oscillations and allowed us to explore the spatial pattern of impacted areas. Our explorations show that the SPM area is more sensitive to oscillations at these periods than the rest of the Newfoundland Shelf. Using idealistic simulations, the current response was outlined for wind periodicities around 2-3 days. Spatially, two response maxima were identified around SPM (north-west of the archipelago and near Burin Peninsula). The relaxation study made it possible to consider the periods of about 2-4 days as a natural period of the system and that this response does not depend on the wind direction around SPM.

These 2-4 day oscillations leave a signature on the sea levels in different harbours on the Newfoundland coast and propagate equatorward. As already shown in several previous studies and in our study, this is the signature of a CSW propagating at a regional scale, with a phase velocity between 16.6 - ~28.8 m s^{-1} (the 'regional CSW'). Our study shows that this regional CSW triggers a 'local CSW' in SPM for periods of between 1.7 to 2.4 days. This local CSW rotates clockwise around SPM with a phase velocity about ~0.7 m s^{-1} and can persist for a few days after the wind event. This 'local CSW' induces currents at these periodicities and accounts for the specificity of this area.

In future studies, a 3D model will be implemented to understand the impact of the summer stratification on these 2-3 day oscillations as they were observed in the summer 1984 (White and Hay, 1994) on the east side of SPM, and north of SPM (Lazure et al., 2018).

Appendixes

Appendix A: List of simulations carried out for this study

Table A1: Characteristics of the runs used to investigate the dynamics

Name of the run	Forcings
A	Tidal and meteorological (wind and pressure) forcings
B	Meteorological forcing (wind and pressure), no tide
E [1:23]	Sinusoidal wind stress (Eq. 3) with varying periods, with no tide
F[1:4]	Wind blowing from the four cardinal directions

Appendix B: Tidal validation

B.1. Tidal validation on sea level

Table B.1: Harmonic analysis of sea levels in the harbours on the Newfoundland and Scotian shelves (from observations and modelling results) computed with T_TIDE (Pawlowicz et al., 2002), for a duration of three months (March, April and May 2014). Bonavista (Bon), Saint John's (StJ), Argentia (Arg), Saint Lawrence (StL), Saint Pierre harbour (StP), Port aux Basques (PaB), North Sydney (NS), Bedford Institute of Oceanography (BIO), Yarmouth (Yar) are the different tide gauges stations used for these computations.

Harbour		O1 amp (cm)	O1 Greenwich phase (°)	K1 amp (cm)	K1 Greenwich phase (°)	M2 amp (cm)	M2 Greenwich phase (°)	S2 amp (cm)	S2 Greenwich phase (°)
Bon	**Obs**	6.9	127.1	7.7	153.1	28.9	313.1	13.8	353.9
	Mod	6.3	129.5	8.5	158.3	33.4	313.0	15.6	347.7
StJ	**Obs**	7.3	129.6	7.3	154.9	33.9	314.7	14.1	0.12
	Mod	7.4	129.2	8.2	165.0	37.8	318.2	16.1	357.6
Arg	**Obs**	8.5	164.0	8.0	172.0	66.6	338.9	18.5	14.3
	Mod	9.1	161.1	6.5	188.3	61.7	340.1	18.3	17.4
StL	**Obs**	8.7	157.0	6.6	187.1	61.6	343.0	17.5	21.2
	Mod	9.3	164.9	6.6	193.2	58.2	343.8	17.0	20.7
StP	**Obs**	8.1	168.6	5.7	205.9	60.5	349.7	17.3	29.4
	Mod	7.9	175.6	5.7	202.4	56.0	348.4	16.2	24.6
PaB	**Obs**	8.7	222.5	7.8	252.7	42.2	13.3	12.5	51.1
	Mod	10.8	219.7	8.8	250.5	38.5	3.8	11.7	39.2
NS	**Obs**	8.3	278.3	7.8	320.5	36.5	352.8	10.8	39.1
	Mod	10.0	270.2	8.7	313.2	38.3	341.9	11.2	22.9
BIO	**Obs**	4.6	86.4	11.2	114.9	63.7	351.0	13.7	24.9
	Mod	4.9	77.6	10.5	115.7	60.5	350.5	13.8	22.8
Yar	**Obs**	10.5	162.9	13.6	177.6	168.0	62.8	27.3	99.7
	Mod	10.3	168.4	12.4	178.8	145.4	64.0	25.5	115.2
A1	**Obs**	7.8	184.0	6.0	193.6	55.5	348.8	16.9	21.1

	Mod	6.7	177.6	6.2	183.5	60.4	347.5	17.7	21.3
A2	**Obs**	8.4	178.5	6.5	188.0	55.6	348.3	16.0	20.7
	Mod	7.8	175.0	7.0	180.9	61.3	346.7	17.0	20.6

B.2 Tidal validation on current velocities

Table B.2: Harmonic analysis on current velocities from ADCP time series (from observations and modelling results) computed T_tide (Pawlowicz et al., 2002), for a duration of three months (March, April and May 2014).

Station		**O1 major axis (ms-1)**	**O1 minor axis (ms-1)**	**O1 orientation**	**O1 Greenwich phase (°)**	**M2 major axis (ms-1)**	**M2 minor axis (ms-1)**	**M2 orientation**	**M2 Greenwich phase (°)**
A1	Obs	0.040	0.001	47.7	169.0	0.059	-0.011	60.9	323.5
	Mod	0.057	-0.002	70.6	176.7	0.037	-0.014	72.4	347.7
A2	Obs	0.101	-0.002	42.4	239.3	0.036	0	53.8	287.6
	Mod	0.092	0	57.5	204.6	0.041	0	60.2	259.5

Station		**K1 major axis (ms-1)**	**K1 minor axis (ms-1)**	**K1 orientation**	**K1 Greenwich phase (°)**	**S2 major axis (ms-1)**	**S2 minor axis (ms-1)**	**S2 orientation**	**S2 Greenwich phase (°)**
A1	Obs	0.042	-0.008	50.3	190.9	0.016	-0.002	49.7	22.6
	Mod	0.037	-0.002	72.2	189.5	0.009	-0.004	75.3	11.8
A2	Obs	0.071	-0.001	43.8	244.2	0.013	0.001	51.0	319.4
	Mod	0.064	0	57.5	204.0	0.018	0	59.4	291.9

B.3. Sea level metrics

Table B.3: Correlation, root mean square error (RMSE eq. 4) and Willmott score (WS eq. 4) computed for the filtered and unfiltered data from observations and model results. These metrics were computed for sea level and current data from tide gauges, ADCP measurements and model results. Bonavista (Bon), Saint John's (StJ), Argentia (Arg), Saint Lawrence (StL), Saint Pierre harbour (StP), Port aux Basques (PaB), North Sydney (NS), Bedford Institute of Oceanography (BIO), Yarmouth (Yar) are the different tide gauges stations used for these computations.

Harbour	**Unfiltered data**			**Filtered data**		
	Correlation	**RMSE (cm)**	**WS**	**Correlation**	**RMSE (cm)**	**WS**
Bon	0.96	12.5	0.95	0.95	4.9	0.74
StJ	0.96	12.1	0.96	0.95	5.5	0.81
Arg	0.98	10.3	0.98	0.83	5.8	0.86
StL	0.98	11.4	0.99	0.98	6.4	0.86
StP	0.99	9.9	0.99	0.97	6.3	0.82
PaB	0.97	9.4	0.98	0.97	4.5	0.83
NS	0.96	12.5	0.96	0.96	4.8	0.74
BIO	0.99	9.0	0.99	0.99	5.7	0.78
Yar	0.99	19.7	0.99	0.98	6.7	0.76

A1	0.97	12.5	0.98	0.87	2.8	0.91
A2	0.99	8.6	0.99	0.81	3.7	0.87
	Correlation	**RMSE (cm/s)**	**WS**	**Correlation**	**RMSE (cm)**	**WS**
U A1	0.62	6.5	0.71	0.63	3.7	0.72
V A1	0.64	8.1	0.78	0.68	4.6	0.82
U A2	0.63	10.9	0.70	0.77	6.0	0.77
V A2	0.67	10.6	0.80	0.81	5.2	0.88

Appendix C: Computation of the lagged correlation

Table C.1: Description of the distances between the different harbours used for the phase velocity estimation. Distance 1 was computed from straight lines and distance 2 with lines following the coast more closely the coast. Bonavista (Bon), Saint John's (StJ), Argentia (Arg), Saint Lawrence (StL), Saint Pierre harbour (StP), Port aux Basques (PaB) are the different tide gauges stations used for these computations.

Harbour Distances (km)		StJ	Arg	StL	StP	PaB
Bon	Distance 1	138.2	336.2	422.6	492.2	729.4
	Distance 2	143.9	383.1	510.5	575.0	1000.4
StJ	Distance 1		198.0	284.4	354.0	591.2
	Distance 2		239.2	366.6	431.1	856.5
Arg	Distance 1			86.4	156.0	393.2
	Distance 2			127.2	191.9	617.3
StL	Distance 1				69.6	306.8
	Distance 2				64.5	489.9
StP	Distance 1					237.2
	Distance 2					425.4

Tableau C.2 Lag in hours obtained by the lagged correlation.

Lag (hours)		StJ	Arg	StL	StP	PaB
Bon	Obs	0.83	5.2	6.0	5.0	8.3
	Mod	0.5	7.0	7.3	6.0	10.2
StJ	Obs		4.5	5.2	4.2	7.3
	Mod		6.2	6.5	5.2	9.2
Arg	Obs			0.8	0	2.83
	Mod			0.3	-1.0	2.7
StL	Obs				-0.7	1.8
	Mod				-1.3	2.3
StP	Obs					2.2
	Mod					3.3

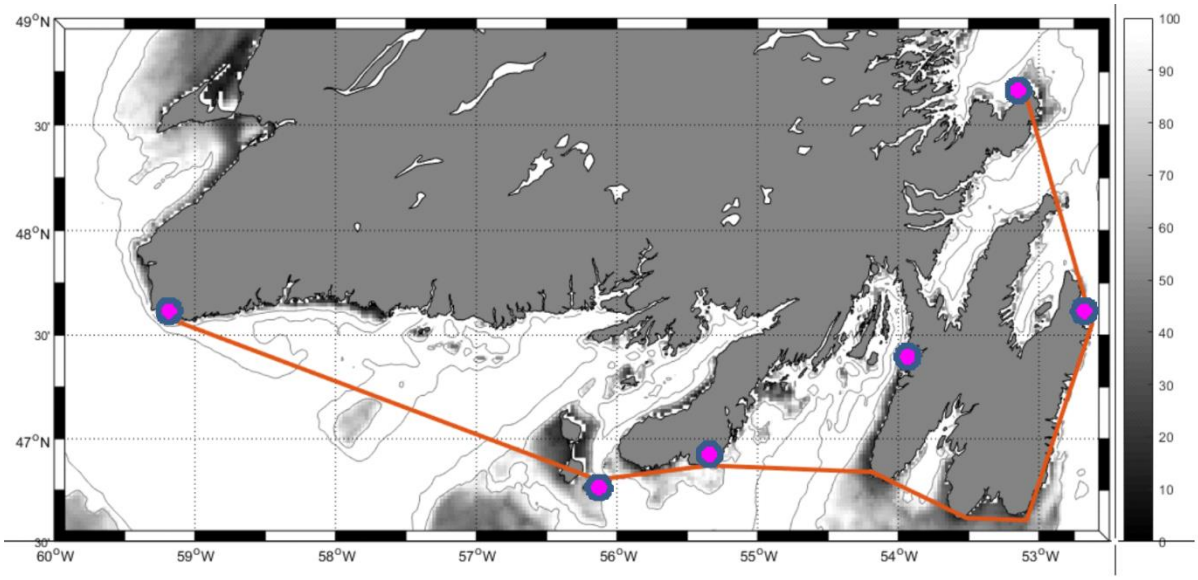

Fig. C.3: Estimation of distance 1 between harbours (located in magenta).

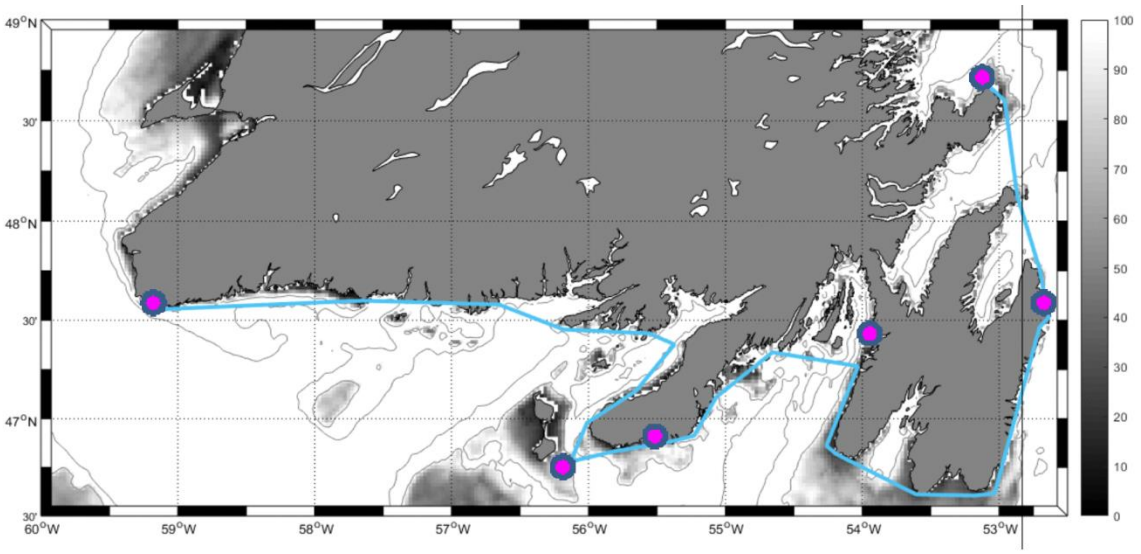

Fig. C.4: Estimation of distance 2 between harbours (located in magenta).

Authors' contributions: MB prepared the manuscript with contributions from all co-authors PL and BLC.

Competing Interest: The authors declare that they have no conflict of interest.

Acknowledgements: The authors would like to thank, Herlé Goraguer, head manager of the IFREMER (Institut Français de Recherche pour l'Exploitation de la Mer) station at St. Pierre for his involvement in this project. We would like to thank also the agents from DTAM (Direction des Territoires, de l'Alimentation et de la Mer) at Saint Pierre and Miquelon, for the deployment of two ADCPs and for recovering their measurements. This project is co-funded by IFREMER and the Ministry of French Overseas Territories. The authors would like to thank Carolyn Engel-Gautier for her help to improve the English of this paper.

References

Bobanović, J., Thompson, K.R., Desjardins, S., Ritchie, H., 2006. Forecasting storm surges along the east coast of Canada and the North-Eastern United States: The storm of 21 January 2000. *Atmos.-Ocean,* 44:2, 151-161, https://doi.org/10.3137/ao.440203.

Brink, K.H., Chapman, D.C., 1987. Programs for Computing Properties of Coastal-Trapped Waves and Wind-Driven Motions Over the Continental Shelf and Slope. *Tech. Rep.* WHOI-87-24.

Chapman, D.C., Beardsley, R.C., 1989: On the Origin of Shelf Water in the Middle Atlantic Bight. *J. Phys. Oceanogr.*, 19, 384–391, https://doi.org/10.1175/1520-0485(1989)019<0384:OTOOSW>2.0.CO;2.

Csanady, G. T. 1981, Circulation in the Coastal Ocean, Part 3, *Eos Trans. AGU*, 62(8), 73– 75, doi:10.1029/EO062i008p00073.

Cyr, F., van Haren, H., Mienis, F., Duineveld, G., Bourgault, D., 2016. On the influence of cold-water coral mound size on flow hydrodynamics, and vice versa. *Geophys. Res. Lett.*, 43, 775–783, https://doi.org/10.1002/2015GL067038.

Donnet, S., Ratsimandresey, A.W., Goulet, P., Doody, C., Bruke, S., Cross, S., 2018. Coast of Bays Metrics: Geography, Hydrology and Physical Oceanography of an Aquaculture Area of the South Coast of Newfoundland. *DFO Can. Sci. Advis. Sec. Res. Doc*. 2017/076.

Dupont, F., Hannah, C.G., Greenberg, D.A., Cherniawsky, J.Y., Naimie, C.E., 2002. Modelling System for Tides for the Northwest Atlantic Coastal Ocean. *Can. Tech. Rep. Hydrogr. Ocean Sci,*. 221: vii + 72pp.

Gordon, R.L., Huthnance, J.M., 1987. Storm-driven continental shelf waves over the Scottish continental shelf. *Cont. Shelf Res.*, 7, 1015–1048.

Grinsted, A., Moore, J.C., Jevrejeva, S., 2004. Application of the cross wavelet transform and wavelet coherence to geophysical time series. *Nonlin. Process. Geophys.*, 11 (5/6), pp.561-566.

Grise, K.M., Son, S.-W., Gyakum, J.R., 2013. Intraseasonal and Interannual Variability in North American Storm Tracks and Its Relationship to Equatorial Pacific Variability. *Mon. Wea. Rev.* 141, 3610–3625. https://doi.org/10.1175/MWR-D-12-00322.1.

Han, G., J.W. Loder, and P.C. Smith, 1999: Seasonal-Mean Hydrography and Circulation in the Gulf of St. Lawrence and on the Eastern Scotian and Southern Newfoundland Shelves. *J. Phys. Oceanogr.*, 29, 1279–1301, https://doi.org/10.1175/1520-0485(1999)029<1279:SMHACI>2.0.CO;2.

Han, G. 2000, Three-dimensional modeling of tidal currents and mixing quantities over the Newfoundland Shelf, *J. Geophys. Res.*, 105(C5), 11407– 11422, doi:10.1029/2000JC900033.

Han, G., and Loder, J. W. 2003, Three-dimensional seasonal-mean circulation and hydrography on the eastern Scotian Shelf, *J. Geophys. Res.*, 108, 3136, doi:10.1029/2002JC001463, C5.

Han, G., Z. Lu, Z. Wang, J. Helbig, N. Chen, and B. de Young, 2008, Seasonal variability of the Labrador Current and shelf circulation off Newfoundland. *J. Geophys. Res.*, 113, C10013, https://doi.org/10.1029/2007JC004376.

Han, G., Paturi, S., de Young, B., Yi, Y., Shum, C.-K., 2010. A 3-D data-assimilative tidal model of the northwest Atlantic. *Atmos.-Ocean*, 48:1, 39-57, https://doi.org/10.3137/OC303.2010.

Han, G., Ma, Z., deYoung, B., Foreman, M., Chen, N., 2011. Simulation of three-dimensional circulation and hydrography over the Grand Banks of Newfoundland. *Ocean Model.,* 40, 199–210. https://doi.org/10.1016/j.ocemod.2011.08.009.

Han, G., Ma, Z., Chen, D., deYoung, B., Chen, N., 2012. Observing storm surges from space: Hurricane Igor off Newfoundland. *Sci. Rep.*, 2, 1010, https://doi.org/10.1038/srep01010.

Hay, A.E., de Young, B., 1989. An oceanographic flip-flop: deep water exchange in Fortune Bay, Newfoundland. *J. Geophys. Res.*, 94:C1, 843–853, https://doi.org/10.1029/JC094iC01p00843.

Hsieh, W.W., Buchwald, V.T., 1985. The Scattering of a Continental Shelf Wave by a Long Thin Barrier Lying Parallel to the Coast. *J. Phys. Oceanogr*., 15, 524–532, https://doi.org/10.1175/1520-0485(1985)015<0524:TSOACS>2.0.CO;2.

Hsieh, W.W., Mysak, L.A., 1980. Resonant Interactions between Shelf Waves, with Applications to the Oregon Shelf. *J. Phys. Oceanogr*., 10, 1729–1741, https://doi.org/10.1175/1520-0485(1980)010<1729:RIBSWW>2.0.CO;2.

Huthnance, J.M., 1974. On the diurnal tidal currents over Rockall Bank. *Deep Sea Res. Oceanogr. Abstr.*, 21(1), 23- 35.

Lazure, P., Dumas, F., 2008. An external–internal mode coupling for a 3D hydrodynamical model for applications at regional scale (MARS). *Adv. Water. Resour.* , 31, 233–250, https://doi.org/10.1016/j.advwatres.2007.06.010.

Lazure, P., Le Cann, B., Bezaud, M., 2018. Large diurnal bottom temperature oscillations around the Saint Pierre and Miquelon archipelago. *Sci. Rep.*, 8(1), 13882 (12p.). https://doi.org/10.1038/s41598-018-31857-w.

LeBlond, P.H., Mysak, L.A., 1981. Waves in the Ocean. *Elsevier, Amsterdam*, 602 pp.

Li, M., Wu, Y., Prescott, R.H., Tang, C.C.L., Han, G., 2015. A modeling study of the impact of major storms on waves, surface and near-bed currents on the Grand Banks of Newfoundland. *J. Geophys. Res. Oceans*, 120, 5358–5386, https://doi.org/10.1002/2015JC010755.

Lyard, F., Lefevre, F., Letellier, T., Francis, O., 2006. Modelling the global ocean tides: modern insights from FES2004. *Ocean Dyn.* 56, 394–415. https://doi.org/10.1007/s10236-006-0086-x.

Ma, Z., Han, G., de Young, B., 2015. Oceanic responses to Hurricane Igor over the Grand Banks: A modeling study. *J. Geophys. Res. Oceans*, 120, 1276–1295. https://doi.org/10.1002/2014JC010322.

Mercer, D., Sheng, J., Greatbatch, R. J., and Bobanović, J. , 2002. Barotropic waves generated by storms moving rapidly over shallow water. *J. Geophys. Res.*, 107(C10), 3152, doi:.

Muller, H., Pineau-Guillou, L., Idier, D., Ardhuin, F., 2014. Atmospheric storm surge modeling methodology along the French (Atlantic and English Channel) coast. *Ocean Dyn.*, 64, 1671–1692. https://doi.org/10.1007/s10236-014-0771-0.

Owens, R.G., Hewson, T.D., 2018. ECMWF Forecast User Guide. https://doi.org/10.21957/m1cs7h.

Pawlowicz, R., Beardsley, B., Lentz, S., 2002. Classical tidal harmonic analysis including error estimates in MATLAB using T_TIDE. *Comput. Geosci.*, 28 (2002), pp. 929-937, https://doi.org/10.1016/S0098-3004(02)00013-4.

Petrie, B.D., 1983. Current response at the shelf break to transient wind forcing. *J. Geophys. Res.*, 88(C14), 9567–9578, https://doi.org/10.1029/JC088iC14p09567.

Plante, M., Son, S.-W., Atallah, E., Gyakum, J., Grise, K., 2015. Extratropical cyclone climatology across eastern Canada. International Journal of Climatology 35, 2759–2776. https://doi.org/10.1002/joc.4170

Sandstrom, H., 1980. On the wind-induced sea level changes on the Scotian shelf, *J. Geophys. Res.*, 85(C1), 461–468, https://doi.org/10.1029/JC085iC01p00461.

Schwing, F.B., 1989. Subtidal response of the Scotian shelf bottom pressure field to meteorological forcing. *Atmos.-Ocean*, 27:1, 157-180, https://doi.org/10.1080/07055900.1989.9649332.

Schwing, F.B., 1992a. Subtidal Response of Scotian Shelf Circulation to Local and Remote Forcing. Part I: Observations. *J. Phys. Oceanogr.*, 22, 523–541, https://doi.org/10.1175/1520-0485(1992)022<0523:SROSSC>2.0.CO;2.

Schwing, F.B., 1992b. Subtidal Response of Scotian Shelf Circulation to Local and Remote Forcing. Part II: Barotropic Model. *J. Phys. Oceanogr.*, 22, 542–563, https://doi.org/10.1175/1520-0485(1992)022<0542:SROSSC>2.0.CO;2.

Sheng, J., Zhai, X., Greatbatch, R.J., 2006. Numerical study of the storm-induced circulation on the Scotian shelf during Hurricane Juan using a nested-grid ocean model. *Prog. Oceanogr.*, 70, 233–254.

Tang, C.L., Gui, Q., DeTracey, B.M., 1998. Barotropic Response of the Labrador/Newfoundland Shelf to a Moving Storm. *J. Phys. Oceanogr.*, 28, 1152–1172,

Thiebaut, S., Vennell, R., 2010. Observation of a Fast Continental Shelf Wave Generated by a Storm Impacting Newfoundland using Wavelet and Cross-Wavelet Analyses. *J. Phys. Oceanogr.*, 40, 417–428, DOI:10.1175/2009JPO4204.1.

Urrego-Blanco, J., Sheng, J., 2012. Interannual Variability of the Circulation over the Eastern Canadian Shelf. *Atmos.-Ocean*, 50:3, 277-300.

Wang, Z., Yashayaev, I., Greenan, B., 2015. Seasonality of the inshore Labrador current over the Newfoundland shelf. *Cont. Shelf Res.* 100, 1–10. https://doi.org/10.1016/j.csr.2015.03.010.

White, M., Hay, A.E., 1994. Dense overflow into a large silled embayment: Tidal modulation, fronts and basin modes. *J. Mar. Res.*, 52(3), 459–487.

Wilkin, J.L., Chapman, D.C., 1987. Scattering of Continental Shelf Waves at a Discontinuity in Shelf Width. *J. Phys. Oceanogr.*, 17, 713–724,.

Willmott, C.J., 1981. On the Validation of Models. *Phys. Geogr.*, 2:2, 184-194, https://doi.org/10.1080/02723646.1981.10642213.

Wright, D.G., Xu, Z., 2004. Double Kelvin waves over the Newfoundland shelf break. *Atmos.-Ocean*,42, 101–111. https://doi.org/10.3137/ao.420202.

Wu, Y., Tang, C.L., Hannah, C., 2012. The circulation of eastern Canadian seas. *Prog. Oceanogr.* 106, 28–48.

Wu, Y., Tang, C.L., Li, M.Z., Prescott, R.H., 2011. Modelling Extreme Storm-Induced Currents over the Grand Banks. *Atmos.-Ocean*, 49, 259–268. https://doi.org/10.1080/07055900.2011.605271.

Xu, Z., Loder, J.., 2004. Data assimilation and horizontal structure of the barotropic diurnal tides on the Newfoundland and southern Labrador shelves. *Atmos.-Ocean*, 42:1, 43-60, DOI: 10.3137/ao.420104